

Politecnico di Torino

Politecnico di Torino

Master's Degree in Aerospace Engineering

A.a. 2025/2026

Graduation Session July 2026

Heat transfer of plasma-swirled impinging jets

Supervisors:
Prof. Jacopo SERPIERI
Prof. Gioacchino CAFIERO
Paolo Joao COMUNIAN

Candidate:
Fabio PEDEMONTE

Abstract

Jet flows impacting on a surface are referred to as Impinging Jets and widely recognized as an efficient method to achieve high heat and mass transfer rates. The addition of an azimuthal component to the stream introduces a swirling motion to a free flow generated by a round nozzle, enhancing turbulent mixing, heat and mass transfer, and flame stabilization, making the swirling jets widely applicable in many engineering fields. The rotational motion is typically achieved by passive methods such as guided vanes or rotating perforated plates. For some applications such as electronics cooling, high values of heat and mass transfer with radial uniformity are requested. While passive techniques are reliable and can achieve high local heat transfer, they can lack on spatial uniformity, introduce flow blockage, and may become less effective if the flow conditions deviate from the design parameters.
In the attempt to mitigate these issues, this study employs active Plasma-based actuators to induce the swirling motion. To evaluate their effectiveness for heat transfer purposes an experimental investigation is carried out by means of quantitative infrared thermography. Four Dielectric Barrier Discharge Plasma Actuators (DBD-PA) were positioned along the axial direction of a quartz cylinder, serving both as the outlet of the jet and the dielectric. The body force produced by this configuration of DBD-PAs induces a tangential acceleration to the axial flow, generating a weak swirling motion. The stream then impinges on a thin foil heated through Joule effect, enabling the evaluation of heat transfer by acquiring two sequences of thermal images and applying the energy balance to the thin foil. The thermal images are acquired with an infrared camera, and the measurement technique is generally known as Quantitative Infrared Thermography (QIRT). Seven nozzle-to-plate distances are tested at Reynolds $Re = 4400$, and the results are set against the corresponding test for a 3D-Printed passive helical multichannel swirler with comparable swirl number. The study demonstrated that the active plasma swirler is capable of enhancing heat transfer with respect to a reference round jet with the same flow conditions (impinging distance, Reynolds number), achieving improvements very close the jet centerline that are comparable to those obtained with the helical passive swirler. Moving away from the stagnation region, however, the heat transfer enhancement provided by the DBD-PA becomes weaker, resulting in lower Nusselt number values than those achieved by the helical insert in the outer radial regions. Despite this limitation, the active swirler produced a more uniform heat transfer distribution across the impingement surface. Moreover, unlike the helical insert, the plasma-based actuation introduced no flow blockage, preserving the favorable characteristics of the round jet while still providing enhanced heat transfer.

Table of Contents

List of Tables IV

List of Figures V

1 Introduction 1
- 1.1 Impinging jets . . . 1
  - 1.1.1 Swirling jets . . . 2
  - 1.1.2 Swirl generation method . . . 5
  - 1.1.3 Heat transfer . . . 8
- 1.2 Plasma actuators . . . 11
  - 1.2.1 Basics of plasma physics . . . 11
  - 1.2.2 Dielectric barrier discharge plasma actuators . . . 16
  - 1.2.3 Electrical characterization . . . 18
- 1.3 Review of literature findings . . . 20
- 1.4 Research goals . . . 22

2 Infrared thermography 24
- 2.1 Quantitative infrared thermography . . . 24
- 2.2 Convective heat transfer model . . . 25
- 2.3 Infrared radiation measurements . . . 26
  - 2.3.1 Radiation heat transfer . . . 27
  - 2.3.2 Infrared cameras . . . 28
- 2.4 Heat flux sensors . . . 29
- 2.5 Data reduction . . . 30

3 Methodology 33
- 3.1 Jet facility . . . 33
- 3.2 Heat transfer measurements . . . 35
  - 3.2.1 Heat flux sensor . . . 36
  - 3.2.2 Infrared camera . . . 40
- 3.3 Swirl generators . . . 40

3.3.1 Passive swirlers 40
3.3.2 Active swirlers 42
3.4 Electrical configuration 43
3.5 Data analysis and reduction 44

4 Results 49
4.1 Methodology validation 50
4.2 Active vs passive swirlers 52
4.2.1 Heat transfer maps 52
4.2.2 Radial Nusselt distribution and standard deviation 55

5 Conclusions 59

A Uncertainty propagation 61

B Nozzle flow characterization 63

C Flow visualization 65

References 68

List of Tables

3.1 Heat transfer characteristics of the materials composing the sensor . 36
3.2 Geometrical and electrical parameters of the heated thin-foil sensor 37
3.3 Geometric parameters of multichannel passive swirl generator . . . 41
3.4 Electrical and swirl parameters of the active swirl generator 42
3.5 Uncertainty contributions for Nusselt number calculation 46

4.1 Flow and actuating conditions for each testcase 49

List of Figures

1.1 Characteristic regions defined for a free jet and an impinging jet . . 2
1.2 Flow structures of an impinging jet for a circular jet (a) and swirled jet (b), reproduced from [3] 3
1.3 Examples of passive devices to induce the swirling motion 6
1.4 DBD plasma actuator active swirl generators 7
1.5 Heat transfer maps of a non-swirling impinging jet at different nozzle to plate distances, adapted from [5] 9
1.6 Influence of Re on the intensity and distribution of heat transfer, reproduced from [5] 10
1.7 Voltage-current curve for DC low pressure electrical discharge tubes 14
1.8 High speed photographs of the DBD discharge in the gas discharge (top) and the arc discharge (bottom), reproduced from [17] 15
1.9 Discharge mechanism in negative and positive corona, reproduced from [18] 15
1.10 Schematic representation of a surface discharge DBD plasma actuator, reproduced from [20] 16
1.11 Sketch of the electric wind generated by plasma actuator operation: wall-jet formation under quiescent air conditions (left), and manipulation of an existing boundary layer (right), reproduced from [16] 17
1.12 Typical arrangements for current and power measurements (a) Shunt resistor technique, (b) induction based technique, (c) shunt capacitor technique, reproduced from [21] 19
1.13 Typical Lissajous figure for a surface discharge DBD PA, reproduced from [20] 20
1.14 Velocity magnitude measured at different z/D planes for active (B, C) and passive (D, E, F, G) swirlers, reproduced from [23] 21
1.15 Heat transfer maps at $Re = 28000$, reproduced from [3] 22

2.1 Local energy balance on the foil element of thickness s 25
2.2 Examples of possible heat flux sensors, reproduced from [27] 29

2.3 Heat fluxes contributing to the local energy balance of the foil element 31

3.1 Section view of the Vitoshinsky nozzle 34
3.2 Section of the feeding line including air filters, fine and coarse pressure regulators and mass flow meter 34
3.3 Jet nozzle with plasma swirler mounted 35
3.4 Sketch of the thermographic experimental setup 35
3.5 3D CAD model of the heat flux sensor 37
3.6 Electrical configuration of the Joule heating system 38
3.7 Heated thin foil heat flux sensor 39
3.8 Sketch of the passive multichannel helical swirler, reproduced from [3] 41
3.9 3D CAD model of the passive multichannel helical insert, reproduced from [22] 42
3.10 Active swirl generator 43
3.11 Components of the GBS Elektronik GmbH Minipuls 4: bridge converter (left) and transformer cascade (right) 43
3.12 Elements of the experimental setup, from top to bottom: oscilloscope, function generator, power supply 44
3.13 Radial distributions Nu for each repeated test compared with the δNu tolerance 47
3.14 Surface distribution of the percentage Nu variation from the mean across the repeated tests 48

4.1 Heat transfer maps for Circular Jet at $Re = 4400$ 50
4.2 Heat transfer maps for Circular Jet at $Re = 16000$ 51
4.3 Azimuthally averaged Nusselt and standard deviation radial profiles for Round Jet at $Re = 4400$ and $Re = 16000$ 52
4.4 Heat transfer maps for Multichannel Passive swirler at $Re = 4400$. 53
4.5 Heat transfer maps for plasma-based active swirler at $Re = 4400$ . . 53
4.6 Heat transfer for the three configurations at $Re = 4400$, $z/D = 2$ with black isoline at $Nu = 50$ 54
4.7 Snapshots at nozzle to plate distance $z/D = 4$. 55
4.8 Surface averaged Nusselt number and percentage standard deviation radial profiles for CJ, MC, and PA 56
4.9 Azimuthally averaged Nusselt number and standard deviation radial profiles for CJ, MC, and PA 57
4.10 Surface averaged Nusselt number over a circular area at fixed radius $r/D = [0.25, 0.5, 2.5]$ as a function of z/D for PA swirler (case B and C), MC and CJ 58

B.1 $V_x - \Delta p$ correlation extended to a wider nozzle pressure drop range (0 to 250 Pa) 64

C.1 Scheme of a Laskin nozzle reproduced from [38] 65
C.2 Laser visualization experimental setup 66
C.3 Images of all investigated cases with laser visualization 67

Chapter 1

Introduction

1.1 Impinging jets

A flow consisting of a jet stream impacting on a surface is defined as an *impinging jet*, and is characterised by the presence of strong velocity gradients, high turbulence levels, and complex interactions between the jet and the impinged surface. Impinging jets are widely employed in industrial and research applications due to their capability to achieve high local heat and mass transfer rates [1]. Applications to engineering fields include turbine blade cooling, paper and fabric drying, furnace heating, tempering of glass and metal sheets, electronic chip cooling, food processing and many others. The basic configuration consists of a jet of fluid issuing from a nozzle and impinging onto a flat or curved surface placed at a distance z from the nozzle exit. The flow behaviour and heat transfer characteristics depend primarily on the geometric and flow parameters, such as the nozzle-to-plate spacing z/D, the Reynolds number Re, and the nozzle geometry.
After exiting the nozzle, if the impinging surface is sufficiently far, the flow first goes through a region where it behaves as a free jet, as depicted in figure 1.1a. This region can be subdivided into a few characteristic zones:

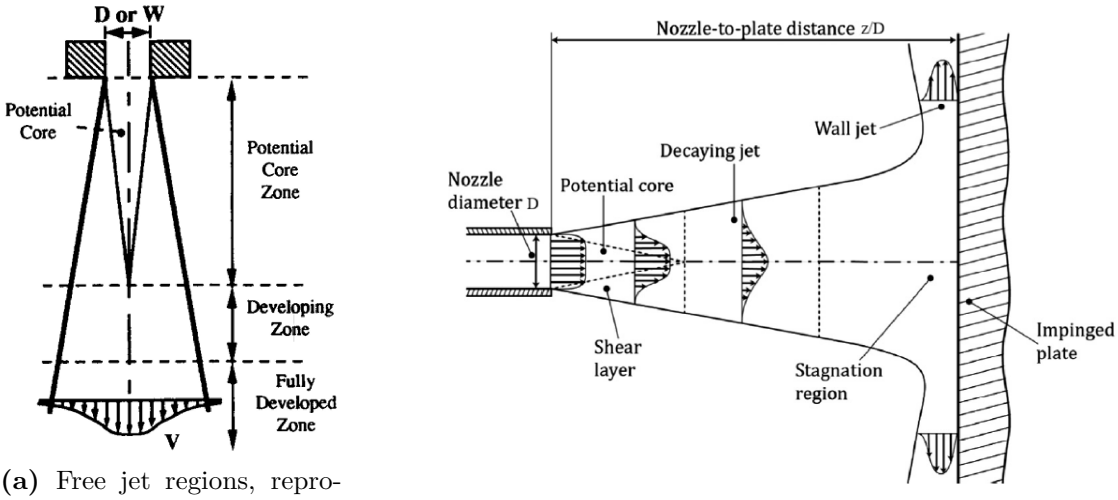
- **Potential core:** in the region immediately downstream of the nozzle exit, the jet velocity profile remains nearly uniform and equal to the exit velocity, with negligible mixing and turbulence growth. Velocity and temperature profiles, as well as turbulence characteristics depend on the upstream conditions and nozzle geometry.

- **Developing region:** the subsequent portion of the jet maintains, in the internal part of the flow, a potential core forming a conical region, and outside of it shear layer instabilities dominate, coherent vortices form and merge, and the jet begins to spread radially.

- **Entrainment region:** the zone surrounding the jet shear layer where ambient fluid is drawn into the jet due to shear-induced vortices, progressively reducing jet momentum and increasing turbulence intensity.

Further down the stream the flow is conditioned by the presence of the impinged surface, creating additional characteristic flow regions shown in figure 1.1b:

- **Stagnation region:** a localised area on the impingement plate directly beneath the jet axis where the flow decelerates to zero normal velocity, pressure peaks, and convective heat transfer coefficients reach their maximum.
- **Wall jet:** Radial outflow formed after the jet impinges and turns along the surface, characterised by a thin, high shear boundary layer that gradually thickens and loses momentum due to viscous dissipation and entrainment.



(a) Free jet regions, reproduced from [2]

(b) Impinging jet regions, adapted from [1]

Figure 1.1: Characteristic regions defined for a free jet and an impinging jet

1.1.1 Swirling jets

A particular kind of jet flows are swirling jets, characterized by an azimuthal velocity component that considerably changes the flow structure, enhances turbulence, mixing, and entrainment, and increases the radial spread of the jet as well as the impinged area. The flow topology of both circular impinging jets and swirled impinging jets shown in figure 1.2 is well documented and depends strongly on various geometrical factors and stream conditions. The addition of the swirl component has long been subject to academic interest due to the improved heat transfer rate

and uniformity over the impinged surface. These enhanced qualities can be relevant for industrial applications such as electronic cooling or chemical vapour deposition [3]. The swirling motion can be obtained through various techniques, including passive methods such as helical insert and guided vanes, or external actuators.

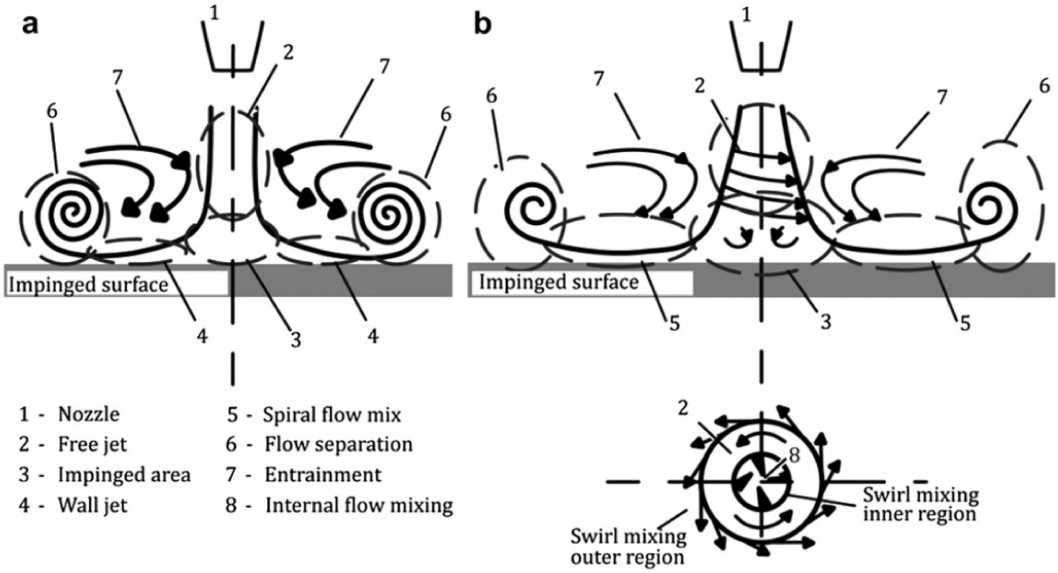


Figure 1.2: Flow structures of an impinging jet for a circular jet (a) and swirled jet (b), reproduced from [3]

Three primary aspects can be defined to characterize a swirling jet:

- **Flow rate**
- **Rotation rate**
- **Swirl generation method**

The swirl generation method plays a fundamental role in the development of the flow structure and characteristics and is analysed in detail in the next section. The first two properties are usually described through dimensionless numbers, respectively the Reynolds number (Re) and the Swirl number (S).
The Reynolds number, which quantifies the flow rate, can be defined in different ways. One possible definition for a jet flow is, as proposed by Billant et al [4]:

$$Re = \frac{\overline{V}_x(x_0)D}{\nu} \tag{1.1}$$

where $\overline{V}_x(x_0)$ is the mean axial velocity at a reference position x_0, D is the nozzle exit diameter, and ν is the kinematic viscosity.

Another equivalent way is to define this dimensionless number utilizing the mass flow rate $\dot{m}$, as implemented in [3]:

$$Re = \frac{4\dot{m}}{\pi \mu D} \tag{1.2}$$

where μ is the dynamic viscosity. This definition can be useful when the mass flow rate measurement is more convenient than a velocity measurement. Circular free jets are typically divided into four characteristic ranges, classified based on the value of their Reynolds number. These ranges are, according to [1]:

- Dissipated laminar jet, $Re < 300$.
- Fully laminar jet, $300 < Re < 1000$.
- Transitional or semi-turbulent jet, $1000 < Re < 3000$.
- Fully turbulent jet, $Re > 3000$.

The Swirl number S, used to characterize the rotational rate, does not have a single formulation due to the complex nature of the phenomena. This dimensionless parameter can be defined in several ways, most commonly as either a velocity ratio or a momentum ratio between the azimuthal and axial flow components.
One common definition expresses the swirl number as a momentum ratio, as reported in [5, 6, 7]:

$$S = \frac{G_\theta}{G_x R} \tag{1.3}$$

where G_θ is the axial flux of azimuthal momentum and G_x is the axial flux of axial momentum, respectively defined as

$$G_\theta = 2\pi\rho \int_0^R r^2 \left(uw + \overline{u'w'} \right) dr \tag{1.4}$$

and

$$G_x = 2\pi\rho \int_0^R r \left(u^2 - \frac{1}{2}w^2 + \overline{u'^2} - \frac{1}{2}\left(\overline{w'^2} + \overline{v'^2} \right) \right) dr \tag{1.5}$$

In eqs. (1.3) to (1.5), R is the nozzle radius, ρ is the fluid density, and r is the radial coordinate. The quantities u, v, and w denote the axial, radial, and tangential components of the velocity vector, respectively, while u', v', and w' represent their corresponding turbulent fluctuations.
According to [6], the Reynolds stress term $\overline{u'w'}$ and the quantity $\overline{u'^2} - \frac{1}{2}(\overline{w'^2} + \overline{v'^2})$ are commonly neglected, since they are assumed to be small compared with the

mean velocity terms and the term u^2, respectively. Under these assumptions, Eqs. (1.4) and (1.5) simplify to

$$G_\theta = 2\pi\rho \int_0^R r^2 uw \, dr \tag{1.6}$$

$$G_x = 2\pi\rho \int_0^R r \left(u^2 - \frac{1}{2} w^2 \right) \, dr \tag{1.7}$$

Thus, the swirl number can be rewritten as

$$S = \frac{\int_0^R r^2 uw \, dr}{R \int_0^R r \left(u^2 - \frac{1}{2} w^2 \right) \, dr} \tag{1.8}$$

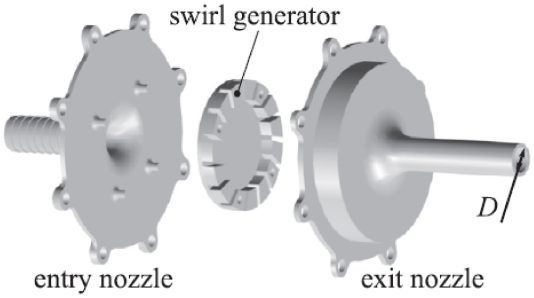
An alternative definition of the swirl number, based on the ratio of azimuthal to axial velocity, is given in [4]:

$$S = \frac{2V_\theta(R/2, x_0)}{V_x(0, x_0)} = \frac{2w(R/2, x_0)}{u(0, x_0)} \tag{1.9}$$

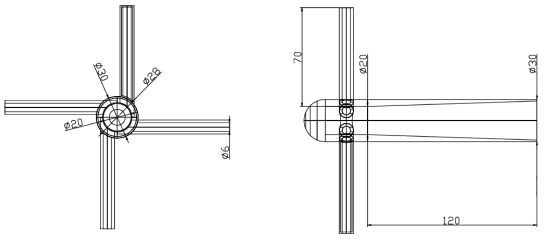
where $2V_\theta(R/2, x_0)$ is the azimuthal velocity measured at half the nozzle radius at the exit plane, and $V_x(0, x_0)$ is the axial velocity measured along the jet axis. This value can be used to classify the jets from weak swirl ($S < 0.3$), moderate swirl ($0.3 < S < 0.6$), and strong swirl ($S > 0.6$).

1.1.2 Swirl generation method

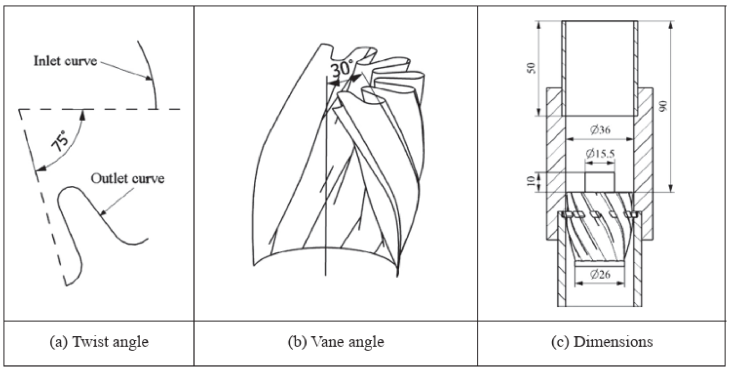
Swirl in impinging jets can be generated through several techniques, ranging from passive to actively controllable methods. The most common passive approaches for swirl generation include the use of guide vanes (fig. 1.3c), the injection of a tangential flow into the nozzle (fig. 1.3b), and the rotation of perforated plates to impart angular momentum to the jet (fig. 1.3a). Guide vanes are typically mounted inside the injector and force the fluid to follow a helical path before exiting the nozzle, generating a controlled swirling motion [3, 8]. Tangential injection systems, on the other hand, introduce one or more secondary streams into the main flow with an azimuthal component, promoting the formation of strong rotational structures [9, 10]. Rotating perforated plates generate swirl mechanically by transferring angular momentum directly to the fluid through the motion of the rotating element [7, 5].
An innovative approach for generating swirling jets through dielectric barrier discharge plasma actuators (DBD PAs) was introduced in [11] and will be analyzed in detail in section 1.2. In this configuration, four pairs of plasma actuators are arranged along the jet axis in order to induce a circumferential velocity component and generate swirl without the use of mechanical inserts or moving parts. This



(a) Rotating plate swirl generator , reproduced from [5]



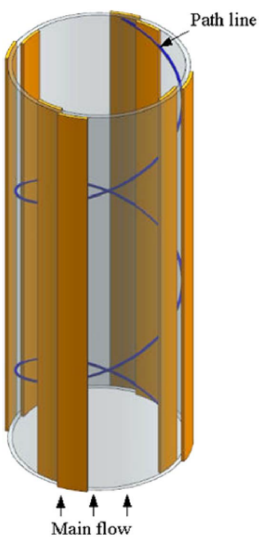
(b) Tangential injection swirl generator, reproduced from [10]



(c) Twisted vanes swirl generator, reproduced from [8]

Figure 1.3: Examples of passive devices to induce the swirling motion

allows active control of the swirl intensity while avoiding the additional pressure losses typically associated with conventional passive swirlers. To electrically isolate the electrodes, a quartz tube was employed as injector material because of its dielectric properties. The actuators themselves consist of pairs of thin copper electrodes positioned on opposite sides of the dielectric surface.
As discussed in [12], plasma swirlers differ significantly from conventional spanwise-oriented plasma actuators. In traditional configurations, fluid particles interact with the plasma region only once while crossing the actuator. In contrast, the axially oriented arrangement of the plasma swirler allows the same fluid particles to be continuously accelerated along their path inside the injector. As a consequence, the azimuthal velocity progressively increases before the flow exits the nozzle, enhancing the resulting swirl intensity. A schematic of the plasma swirler proposed in [11] and further investigated in [12] is reported in figure 1.4a, together with the trajectory followed by the fluid particles in the vicinity of the actuators.



(a) Straight electrodes generator, reproduced from [12]



(b) Helical electrodes generator, reproduced from [13]

Figure 1.4: DBD plasma actuator active swirl generators

An important result highlighted in [12] is that the swirl number increases approximately linearly with electrode length, reaching its maximum value near the actuator exit. However, plasma swirlers based on straight electrodes suffer from non-uniform plasma distribution along the injector wall, potentially reducing the effectiveness of the flow control action. Despite advantages such as reduced power consumption, relatively high tangential velocity generation, and simpler manufacturing, these limitations motivated the development of alternative configurations.

To address these issues, a helical electrode plasma swirler was proposed in [13] and shown in figure 1.4b. In this design, the DBD actuators are arranged following a helical pattern around the injector surface, producing a more uniform plasma distribution and improved circumferential forcing. Furthermore, the helical configuration can also be combined with conventional passive swirlers. Experimental investigations demonstrated that the use of helical electrodes promotes the formation of a wider central recirculation zone compared with straight electrode configurations, indicating a stronger and more spatially distributed swirling motion.

1.1.3 Heat transfer

A submerged jet impinging on a surface exchanges energy with said surface by means of convective heat transfer, with intensity and spatial distribution depending on the flow characteristics. Convective heat transfer follows Newton's Law (Eq. 1.10) and is proportional to the *convective heat transfer coefficient* h_c:

$$q_c'' = h_c \Delta T \tag{1.10}$$

This quantity is usually reported in terms of dimensionless Nusselt number Nu, which is defined from h_c as:

$$Nu = \frac{h_c L}{\kappa_a} \tag{1.11}$$

where L is a characteristic length scale of the problem and κ_a is the thermal conductivity of air. The Nusselt number represents the ratio between convective and conductive heat transfer and provides a convenient way to compare heat transfer results obtained under different operating conditions and geometrical scales.
Since the convective heat transfer coefficient is directly related to the exchanged convective heat flux through Newton's law of cooling, the Nusselt number is also proportional to the local convective heat transfer intensity:

$$Nu \propto h_c \propto q_c'' \tag{1.12}$$

Heat transfer intensity and distribution of a circular jet impinging on a flat surface strongly depends on the impinging distance and Reynolds number of the flow. The nozzle to plate spacing z/D not only affects the overall heat transfer intensity, but also significantly modifies the spatial distribution of the Nusselt number. For distances greater than 4-6 nozzle diameters, the heat transfer profile shows a single bell-shaped curve with a strong central peak at the jet axis, where the stagnation point is located. In this flow regime, the jet has sufficient space to develop before impinging on the target surface, allowing the velocity field and turbulence structures to evolve more uniformly. This leads to a strong heat transfer near the centerline of

the jet, and moving away from the stagnation region, the radial wall jet progressively loses momentum and the Nusselt number decreases monotonically with increasing radial distance. For shorter distances, the distribution is characterized by the presence of ring-shaped zones of maximum and minimum values along the radial direction as highlighted by the results of Paolillo et al [5] reported in figure 1.5. At these short nozzle-to-plate distances, two peaks can arise, driven by two different formation mechanisms. The Inner peak is associated with the radial acceleration of the flow turning around the stagnation point and consequent thinning of the local boundary layer. The radial acceleration distribution is primarily influenced by the velocity profile of the incoming jet and by the pressure field developing in the stagnation region. Therefore, the inner peak is mostly found when high power or uniform velocity profiles are used. These conditions are likely met at short impinging distances, to which, in fact, is usually associated the inner peak. The outer peak is correlated with enhanced turbulence fluctuations in the wall boundary layer, caused by secondary vortical structures generated from the primary jet shear layer vortices when these penetrate sufficiently close to the wall. The vortex ring surrounding the jet is responsible for the second Nusselt number peak that can be considered a result of flow reattachments after flow separation and not of a simple transition from laminar to turbulent flow [1].

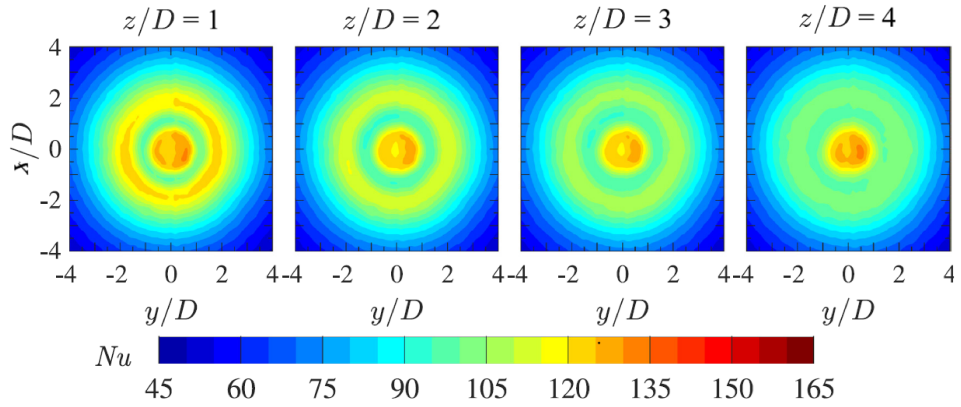


Figure 1.5: Heat transfer maps of a non-swirling impinging jet at different nozzle to plate distances, adapted from [5]

Differently, variations in Reynolds number have only a limited influence on the overall shape of the heat transfer distribution, which remains governed primarily by the flow topology and nozzle-to-plate spacing. However, increasing Re leads to a substantial enhancement of the convective heat transfer coefficient h_c, and consequently of the Nusselt number.
The increase in heat transfer is associated with the larger momentum of the impinging flow and the corresponding intensification of mixing and turbulence

levels within the jet. As a result, higher Reynolds numbers produce greater heat transfer rates over the entire impingement region. Nevertheless, the Nusselt number distributions do not simply scale proportionally with Reynolds (fig 1.6). Experimental observations show that, as Re increases, the radial decay of Nu becomes progressively steeper, indicating that the enhancement of heat transfer is concentrated predominantly in the vicinity of the stagnation region [5]. Therefore, higher Reynolds numbers not only increase the magnitude of heat transfer, but also modify its spatial distribution, resulting in stronger yet more localized heat transfer peaks.

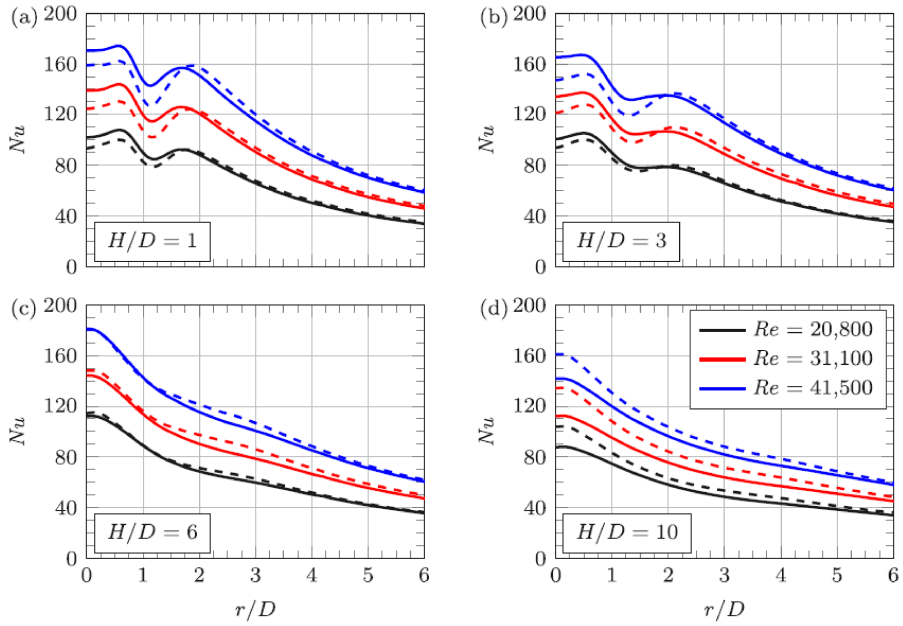


Figure 1.6: Influence of Re on the intensity and distribution of heat transfer, reproduced from [5]

The introduction of swirl significantly alters both the flow field and the resulting heat transfer distribution of an impinging jet. In general, increasing the swirl intensity weakens the heat transfer at the stagnation point while enhancing radial transport and mixing. Consequently, heat transfer tends to be redistributed over a larger portion of the impingement surface, resulting in more uniform Nu distributions. The beneficial effect of swirl on the area-averaged Nusselt number is generally most pronounced for intermediate nozzle-to-plate spacings ($z/D \approx 3{-}6$), whereas smaller gains are observed at very low or very large values of z/D.

For weak swirl conditions ($S < 0.3$), the heat transfer maps remain nearly axisymmetric and closely resemble those of a non-swirling jet. At larger nozzle-to-plate distances ($z/D > 6$), only a modest reduction of the stagnation point Nusselt

number is typically observed. Nevertheless, the enhanced radial mixing generated by the azimuthal velocity component generally produces a slight increase in the area-averaged Nusselt compared with the non-swirling case.
At moderate swirl levels ($0.3 < S < 0.6$), the effects of swirl become more evident. For nozzle-to-plate spacings in the range $z/D \approx 3{-}6$, the stagnation point heat transfer decreases by approximately $10{-}20\%$, while annular regions of elevated Nusselt number appear around $r/D \approx 2$. These secondary peaks are associated with increased interaction between the wall boundary layer and vortical structures originating from the jet shear layer. The resulting redistribution of heat transfer over a wider surface area leads to a significant increase in the area-averaged Nusselt number, typically of the order of $10{-}15\%$.
For strong swirl conditions ($S > 0.6$), the flow structure can be dramatically modified. At small nozzle-to-plate distances ($z/D < 3$), vortex breakdown may occur before the jet reaches the impingement surface, causing the disappearance of the central heat transfer peak and the formation of annular regions of maximum Nu. Under these conditions, the heat transfer distribution becomes considerably more uniform, although the stagnation point Nusselt number may decrease by as much as 30%. Despite this local reduction, the area averaged heat transfer often exhibits the largest improvement, reaching increases of up to $20{-}25\%$, as the enhancement in turbulent mixing and radial transport outweighs the reduction in axial momentum.

1.2 Plasma actuators

In recent years, plasma actuators have attracted considerable interest in the field of active flow control owing to their distinctive advantages over conventional actuation techniques. Their simple construction, low power consumption, fast dynamic response, and absence of moving mechanical components make them an attractive solution for a broad range of applications, including aerodynamic flow control, heat transfer enhancement, and industrial processes. This chapter introduces the fundamental physical principles underlying plasma generation and gas discharges, before describing the operating principle and configuration of Dielectric Barrier Discharge Plasma Actuators.

1.2.1 Basics of plasma physics

Plasma is commonly referred to as the fourth state of matter and is formed when sufficient energy is supplied to a gas to ionize its constituent atoms or molecules. The resulting medium consists of free electrons, positive and negative ions, neutral particles, and excited species. Owing to the presence of charged particles, plasma

exhibits electrical conductivity and responds to externally applied electromagnetic fields.
Despite containing free charges, plasma is macroscopically electrically neutral. This property, known as quasi-neutrality, implies that the densities of positive and negative charges are approximately equal,
Depending on the thermodynamic equilibrium between its constituent particles, plasma can be classified as either thermal or non-thermal. In thermal plasmas, electrons, ions, and neutral particles are in local thermodynamic equilibrium and therefore possess nearly the same temperature,

$$T_e \approx T_i \approx T_n. \tag{1.13}$$

In contrast, non-thermal plasmas, are characterized by a significantly higher electron temperature than that of the ions and neutral gas ($T_e \gg T_n$). Since temperature is related to the average kinetic energy of a species,

$$\langle E_k \rangle = \frac{3}{2} k_B T, \tag{1.14}$$

where k_B is the Boltzmann constant, the much lower mass of electrons results in substantially higher thermal velocities. Consequently, electrons sustain the plasma discharge and are primarily responsible for generating the electrohydrodynamic (EHD) body force.
The behavior of non-thermal plasmas is characterized by several key parameters. One of these is the Debye length, which defines the spatial extent over which charge imbalances can exist:

$$\lambda_D = \sqrt{\frac{\varepsilon_0 k_B T_e}{n_e e^2}}, \tag{1.15}$$

where ε_0 is the vacuum permittivity, n_e is the electron number density, and e is the elementary charge. For a gas to exhibit plasma behavior, the Debye length must remain much smaller than the characteristic dimension of the system ($\lambda_D \ll L$), ensuring quasi neutrality throughout the plasma.
Another important parameter is the degree of ionization,

$$\alpha = \frac{n_i}{n_i + n_n}, \tag{1.16}$$

where n_i and n_n denote the ion and neutral particle number densities, respectively. Plasma actuators operate in a weakly ionized regime ($\alpha \ll 1$), where collisions between charged and neutral particles dominate the plasma dynamics.
When an external electric field E is applied, charged particles acquire a drift velocity given by

$$\mathbf{v}_d = \pm\mu\mathbf{E}, \tag{1.17}$$

where μ is the particle mobility. Through frequent collisions, the drifting charged particles transfer momentum to the surrounding neutral molecules, generating the electrohydrodynamic body force responsible for inducing airflow. This momentum transfer mechanism constitutes the fundamental operating principle of flow control strategies based on plasma actuators.
The formation of plasma requires the electrical breakdown of a gas. Under normal conditions, gases behave as electrical insulators because only a very small number of naturally occurring charged particles are present. When an electric field is applied between two electrodes, free electrons are accelerated and may acquire sufficient kinetic energy to ionize neutral molecules through collisions,

$$e^- + A \rightarrow 2e^- + A^+, \tag{1.18}$$

where A denotes a neutral gas molecule. The newly generated electrons are subsequently accelerated by the electric field, producing additional ionization events and initiating an avalanche process known as the Townsend discharge.
The voltage required to initiate electrical breakdown depends primarily on the gas pressure p and the electrode spacing d. This relationship is described by Paschen's law,

$$V_b = \frac{B\,pd}{\ln(A\,pd) - \ln\left[\ln\left(1 + \frac{1}{\gamma_{se}}\right)\right]}, \tag{1.19}$$

where A and B are gas-dependent constants and γ_{se} is the secondary electron emission coefficient. Paschen's law predicts the existence of a minimum breakdown voltage corresponding to an optimal value of the product pd. At low pressures, electrons undergo too few collisions to sustain ionization, whereas at excessively high pressures their mean free path becomes too short to gain sufficient energy between successive collisions [14].
Following electrical breakdown, different discharge regimes may develop depending on the applied voltage and current. At low current levels, localized *corona discharges* are formed near regions of high electric field intensity. As the current increases, the discharge evolves into a stable *glow discharge*, characterized by a nearly uniform plasma and limited gas heating. Further increases in current eventually produce an *arc discharge*, where intense Joule heating results in high gas temperatures and substantial electrode erosion. The characteristic current-voltage curve can be obtained with low pressure discharge tube by gradually increasing the applied voltage, V, while measuring the corresponding discharge current, I, as illustrated schematically in figure 1.7

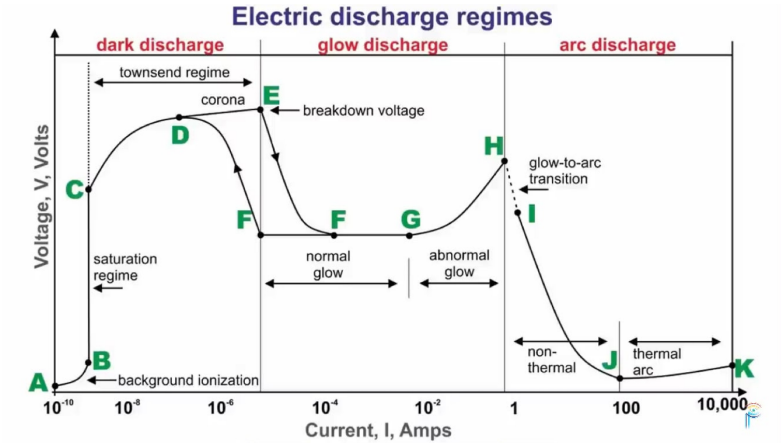


Figure 1.7: Voltage-current curve for DC low pressure electrical discharge tubes

Different configurations of the electrodes and voltage application strategies lead to different types of electrical discharge used to generate the plasma, resulting in the development of Plasma Actuators of different kinds. Among the most common configurations are Direct Current Corona Discharge (DC-corona) actuators, Alternating Current Dielectric Barrier Discharge (AC-DBD) actuators, Nanosecond Pulsed Dielectric Barrier Discharge (ns-DBD) actuators, and Localized Arc Filament Plasma Actuators (LAFPA) [15, 16]. DC-corona actuators operate by applying a high direct-current voltage between asymmetric electrodes, producing a corona discharge that generates an EHD body force capable of inducing a steady ionic wind. Although they can produce relatively strong body forces, their operation requires exposed electrodes and is generally limited by ozone production, electrode degradation, and the risk of transition to arc discharges.

Alternating Current Dielectric Barrier Discharge actuators employ two electrodes separated by a dielectric barrier and energized by a high voltage alternating signal. The dielectric layer suppresses the formation of continuous arcs by limiting the discharge current, allowing stable operation at atmospheric pressure while generating a surface plasma and a near-wall electric wind. Owing to their simple construction, low power consumption, fast response, and absence of moving parts, AC-DBD actuators have become the most widely adopted plasma actuators for active flow control applications. Nanosecond Pulsed Dielectric Barrier Discharge actuators share a similar electrode configuration with AC-DBD devices but are driven by high-voltage pulses with durations of only a few nanoseconds. Rather than generating a continuous ionic wind, these actuators produce rapid localized gas heating, creating pressure waves and vortical structures that are particularly effective for high-speed and compressible flow applications. Localized Arc Filament Plasma Actuators operate through repetitive arc discharges established between

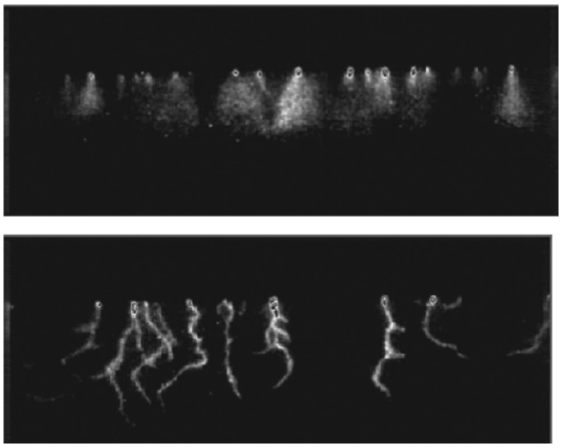


Figure 1.8: High speed photographs of the DBD discharge in the gas discharge (top) and the arc discharge (bottom), reproduced from [17]

closely spaced electrodes. In contrast to DBD actuators, LAFPAs intentionally generate localized thermal perturbations and pressure fluctuations that can effectively excite flow instabilities, making them particularly suitable for the control of free shear layers and high-speed jets. However, their higher power consumption and localized heating generally limit their applicability compared with DBD-based devices. Among these technologies, AC-DBD plasma actuators have received the greatest attention for low speed aerodynamic flow control owing to their robustness, low energy requirements, and ability to generate a controllable electrohydrodynamic body force without significant heating of the surrounding fluid. For these reasons, the present work focuses exclusively on AC-DBD plasma actuators.

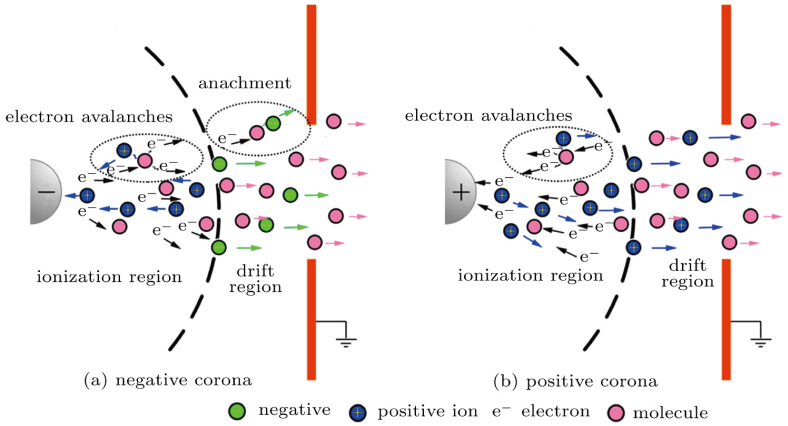


Figure 1.9: Discharge mechanism in negative and positive corona, reproduced from [18]

1.2.2 Dielectric barrier discharge plasma actuators

Dielectric Barrier Discharge Plasma Actuators are among the most widely investigated devices for active flow control. Since their introduction for aerodynamic applications in the late 1990s, they have attracted considerable interest due to their simple construction, rapid response, absence of moving mechanical parts, and relatively low power consumption [19, 15, 16]. Unlike conventional flow control devices based on synthetic jets or mechanical actuators, DBD plasma actuators modify the surrounding flow through the direct interaction between an electric field and the working fluid. DBD PAs can be broadly classified into two main configurations: volume discharge (VD) and surface discharge (SD). In VD actuators, the plasma is generated between two electrodes separated by a dielectric barrier, whereas in SD actuators the electrodes are placed on opposite sides of the dielectric, causing the discharge to develop along its surface.

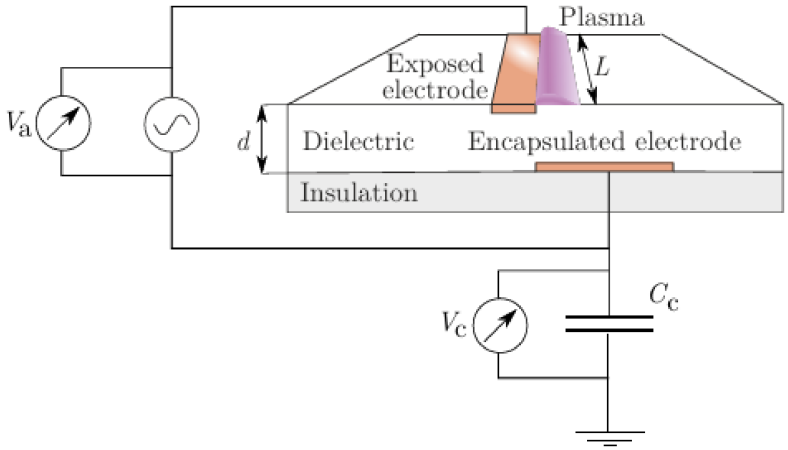


Figure 1.10: Schematic representation of a surface discharge DBD plasma actuator, reproduced from [20]

A conventional surface DBD plasma actuator consists of two thin metallic electrodes separated by a dielectric material. The lower electrode is completely embedded in the dielectric and connected to ground, whereas the upper electrode is exposed to the surrounding air and supplied with a high voltage alternating current. Once the applied voltage exceeds the breakdown threshold, a surface plasma discharge develops over the dielectric in the vicinity of the exposed electrode. Typical operating conditions involve voltages ranging from 1 up to 50 kV and excitation frequencies from a 0.5 to 25 kilohertz. Common dielectric materials include Kapton, Teflon, glass, quartz, ceramics and Plexiglas, with thicknesses typically ranging from 0.1 to a few millimetres, while the electrodes are generally fabricated from thin copper or aluminium foils. Owing to their layered construction, DBD actuators can

be mounted directly onto aerodynamic surfaces with minimal geometric intrusion. Figure 1.10 illustrates the typical configuration of a conventional surface DBD plasma actuator. During each half cycle of the applied AC voltage, the electric field near the exposed electrode exceeds the gas breakdown threshold, generating a surface dielectric barrier discharge. The dielectric layer prevents the formation of a continuous arc by accumulating surface charges that locally oppose the applied electric field, rapidly extinguishing each discharge event. Consequently, the plasma consists of a large number of short-lived microdischarges or streamers occurring in rapid succession rather than a continuous discharge channel [15, 16, 19]. The characteristics of these microdischarges differ during the positive and negative half-cycles of the applied voltage owing to the different evolution of surface charge accumulation on the dielectric [19].
Although electrons initiate the ionization process, their contribution to the momentum transfer is negligible because of their very small mass. Instead, the ions accelerated by the electric field collide with the surrounding neutral air molecules, transferring momentum through successive collisions. This interaction generates an EHD body force that acts predominantly parallel to the dielectric surface and accelerates the surrounding fluid. The volumetric force can be expressed as

$$\mathbf{f}_{\mathrm{EHD}} = \rho_e \mathbf{E}, \tag{1.20}$$

where ρ_e is the space charge density and E is the local electric field. Under atmospheric pressure DBD operating conditions, this Coulomb force represents the dominant contribution to the total body force, while pressure gradient and electrostrictive effects are generally negligible [15].

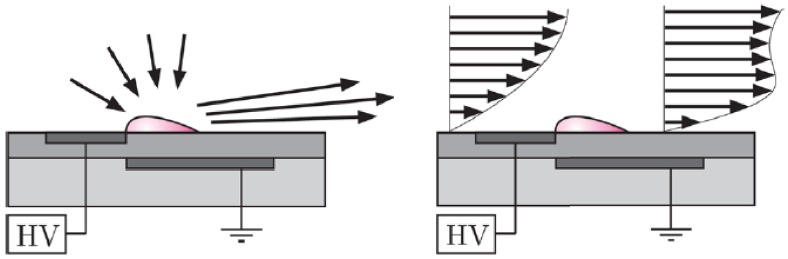


Figure 1.11: Sketch of the electric wind generated by plasma actuator operation: wall-jet formation under quiescent air conditions (left), and manipulation of an existing boundary layer (right), reproduced from [16]

The momentum imparted by the EHD body force produces a thin wall jet commonly referred to as the *electric wind*. As depicted in the sketch in figure 1.11, in quiescent air, this induced flow develops tangentially to the dielectric surface, whereas in the presence of an external flow it transfers momentum to the boundary layer, modifying its velocity distribution. Since DBD actuators inject momentum without

introducing additional mass into the flow, they are commonly classified as zero net mass flux actuators [16]. Typical induced velocities range from approximately 3 to 8 m/s, depending on the applied voltage, excitation frequency, electrode geometry and dielectric properties [15, 19].

The performance of DBD plasma actuators is strongly influenced by both electrical and geometrical parameters. Increasing the applied voltage generally increases the plasma extension, electrical power consumption, and induced body force. Similarly, the excitation frequency, electrode dimensions, electrode overlap, dielectric thickness, and dielectric permittivity all influence the discharge characteristics and the resulting induced flow. Consequently, numerous studies have focused on optimizing the actuator geometry to maximize the generated momentum while maintaining discharge stability.

Despite their numerous advantages, conventional DBD PAs provide a relatively limited momentum authority compared with mechanical flow control devices, causing their effectiveness to decrease as the free stream velocity increases. Nevertheless, their fast response, compact design, robustness, and ability to operate at atmospheric pressure without moving parts continue to make them an attractive solution for active flow control, including separation control, transition delay, mixing enhancement, noise reduction, heat transfer augmentation, and, more recently, swirl generation [15, 16, 19].

1.2.3 Electrical characterization

The operation of AC-DBD plasma actuators requires high voltage, high frequency electrical signals. Although the applied voltage has a period on the order of milliseconds, the plasma consists of a large number of microdischarges occurring over micro- or nanosecond timescales. Consequently, the electrical characterization of DBD actuators is challenging, particularly due to the difficulty of accurately measuring the highly transient discharge current.

The electrical performance of a DBD plasma actuator is commonly assessed through its power consumption. Three approaches are generally adopted: the resistor method, that directly measures the current, an induction-based method, in which the current is measured using a Rogowski coil, and the capacitor method, where the charge transferred through the actuator is determined from the voltage across a known capacitor connected in series with the grounded electrode [15, 19, 21]. The electrical circuits employed for these measurement methods are shown in Figure 1.12. Owing to its superior signal-to-noise ratio and its ability to account for all the microdischarge events without requiring extensive signal filtering, the capacitor method was adopted in the present work.

The instantaneous charge accumulated on the probe capacitor is obtained as

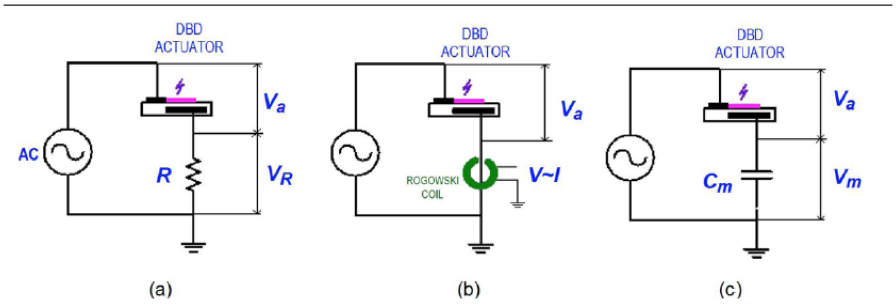


Figure 1.12: Typical arrangements for current and power measurements (a) Shunt resistor technique, (b) induction based technique, (c) shunt capacitor technique, reproduced from [21]

$$Q_m(t) = C_p V_m(t), \tag{1.21}$$

where C_p is the probe capacitance and $V_m(t)$ is the measured capacitor voltage. Since the capacitor is connected in series with the actuator, the same current flows through both components, allowing the instantaneous electrical power to be expressed as

$$P_a(t) = V_a(t) \cdot I_a(t) = V_a(t) \cdot C_p \frac{dV_m(t)}{dt}, \tag{1.22}$$

where $V_a(t)$ and $I_a(t)$ are respectively the voltage and current applied to the actuator.
The average power consumed over one actuation period T is therefore

$$P = \frac{1}{T} \oint V_a \, dQ_m, \tag{1.23}$$

which corresponds to the area enclosed by the charge–voltage (Q-V) diagram, commonly referred to as the *Lissajous figure* (Figure 1.13). Besides providing the average electrical power, the Lissajous curve also offers qualitative information on the electrical behaviour of the actuator, such as its effective capacitance during plasma formation.
To ensure accurate power measurements, the probe capacitor must be carefully selected. Since the actuator and the probe capacitor are connected in series,

$$\frac{1}{C_{\text{tot}}} = \frac{1}{C_a} + \frac{1}{C_p}, \tag{1.24}$$

the capacitance C_p should be sufficiently larger than the actuator capacitance C_a to avoid modifying the electrical characteristics of the circuit, while remaining low enough to maintain an adequate signal-to-noise ratio. The appropriate capacitance

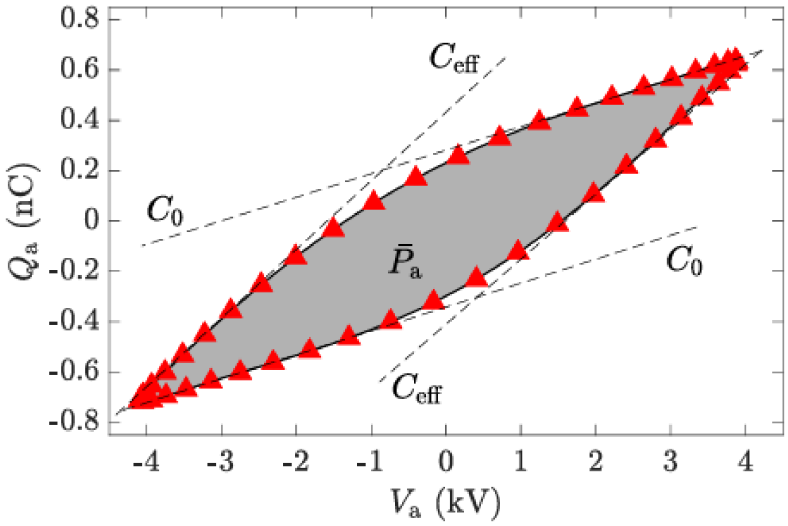


Figure 1.13: Typical Lissajous figure for a surface discharge DBD PA, reproduced from [20]

range can be identified by verifying that the measured power becomes independent of the selected probe capacitance, as reported in the literature [15, 20].

1.3 Review of literature findings

This work builds on previous studies on DBD-PA swirl generators and heat transfer of swirling jets.
Regarding plasma-based swirl generation, constituting the foundation of the present work are the two previous master's theses conducted in the Modesto Panetti Laboratory [22, 23]. The first demonstrated the feasibility of generating swirling jets using Dielectric Barrier Discharge Plasma Actuators as an active alternative to conventional passive swirl generators. Four plasma actuators, uniformly distributed around the circumference of a dielectric nozzle, were shown to impart a tangential velocity component to the jet, producing measurable swirl while allowing the swirl intensity to be actively controlled through the electrical operating conditions.
Building upon these findings, [23] provided a more comprehensive aerodynamic characterization of plasma-generated swirling jets through stereoscopic Particle Image Velocimetry measurements. Figure 1.14 reports some of the results obtained by Putignano in this investigation. The generated flow was quantitatively compared with passive swirl generators by evaluating the swirl number together with the axial, radial, and tangential velocity distributions. The study showed that improvements in the actuator design and electrical characterization enabled swirl numbers comparable to those produced by conventional multichannel swirlers under

low Reynolds number conditions.

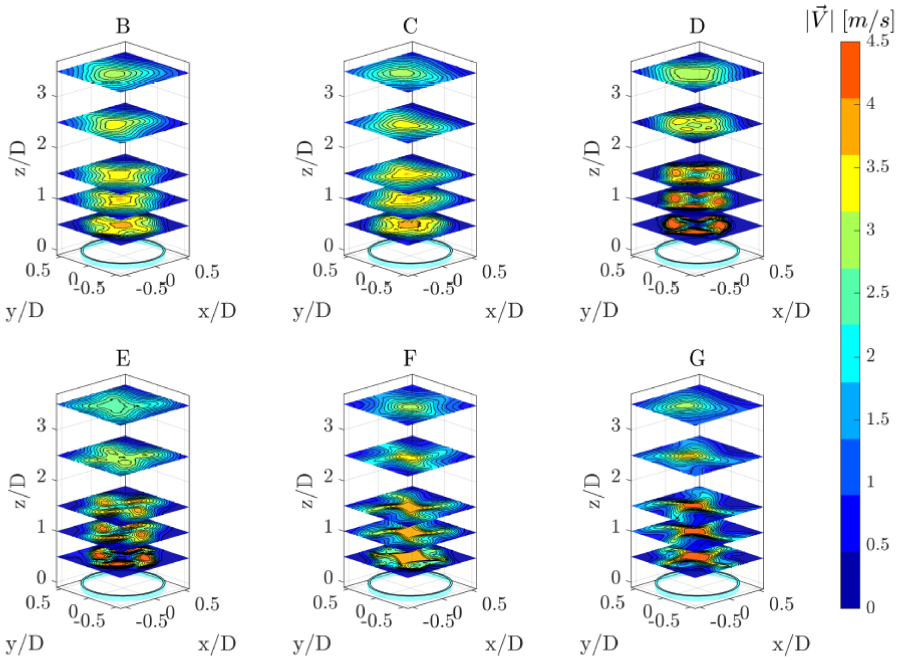


Figure 1.14: Velocity magnitude measured at different z/D planes for active (B, C) and passive (D, E, F, G) swirlers, reproduced from [23]

However, the effectiveness of plasma actuation decreased as the jet Reynolds number increased, since the azimuthal momentum introduced by the actuators became progressively smaller relative to the axial momentum of the flow.
Overall, these studies established the feasibility of DBD-PAs as active swirl generators and provided a detailed characterization of the resulting flow field. Nevertheless, their investigations were limited to the aerodynamic behavior of free jets, leaving the influence of plasma generated swirl on impinging jet heat transfer unexplored. This aspect constitutes the main motivation for the present work.
Regarding the heat transfer performance of swirling impinging jets, the study by Ianiro and Cardone [3] constitute the main reference for the present work. Using infrared thermography in combination with the heated thin-foil technique, they experimentally investigated the influence of swirl intensity on the convective heat transfer distribution of a single impinging jet generated by passive helical inserts. The experiments were performed over a range of swirl numbers and nozzle-to-plate distances, providing a comprehensive characterization of both the heat transfer rate and its spatial uniformity.
Their results, reported in figure 1.15, showed that increasing the swirl number promotes a progressive broadening of the impingement region, leading to a more

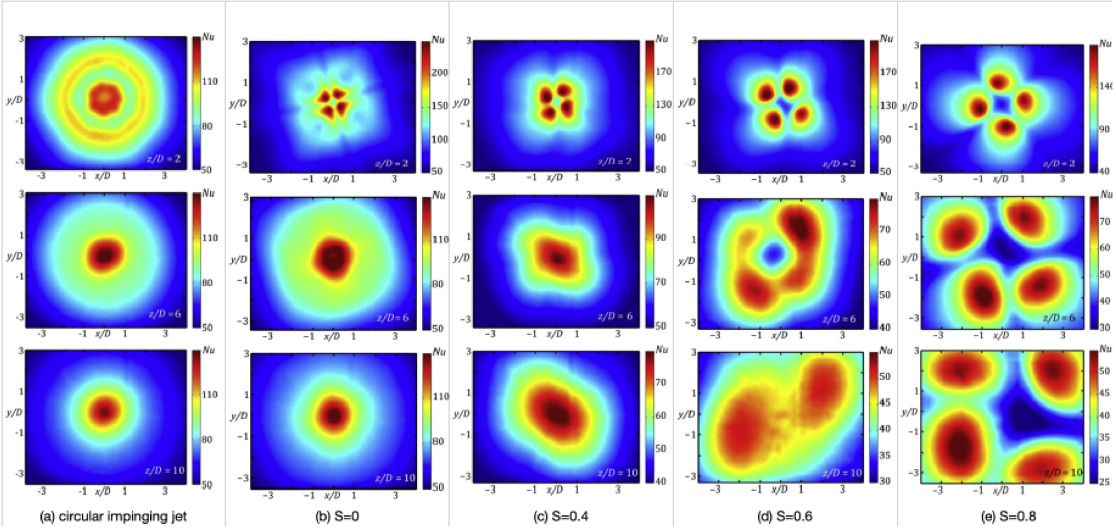


Figure 1.15: Heat transfer maps at $Re = 28000$, reproduced from [3]

uniform heat transfer distribution, particularly at larger nozzle-to-plate distances. This improvement in uniformity, however, is accompanied by a reduction in the average heat transfer rate due to the weakening of the axial momentum caused by the tangential velocity component. For sufficiently high swirl numbers, the onset of vortex breakdown generates a central low heat transfer region associated with the formation of a recirculation zone.
The experimental methodology adopted in the present work closely follows that used in [3]. The same heated thin-foil infrared thermography technique and a geometrically equivalent multichannel passive swirler were employed to allow a direct comparison with the literature and between passive and active methods.

1.4 Research goals

Swirling jet flows have been proven to be an effective method for enhancing heat transfer on an impinging surface. Passive inserts have traditionally been used as swirl generation method thanks to their reliability, but they can introduce pressure losses, flow blockage and fixed operating conditions. These limitations have motivated the search for active flow control strategies capable of generating or modifying swirl.
Thanks to their absence of moving parts, low weight, low power consumption, and controllable operating characteristics, DBD plasma actuators have emerged as an effective solution for active flow control. Despite their widespread use in a variety of applications, studies investigating the generation of an azimuthal

velocity component in a conventional round jet using DBD-PAs remain relatively scarce. Building on the knowledge of the velocity fields and electrical characteristics obtained in the works of the previous master's theses [23, 22], this work aims to evaluate the heat transfer capabilities of swirling jets generated by DBD Plasma actuators
To achieve this, the following goals have been identified:

- Design of a heated thin-foil sensor that works both as the impinged surface and the heat flux sensor;
- Reconfiguration of the jet facility to allow Quantitative Infrared Thermography (QIRT) measurements;
- Evaluation of Nusselt number distributions over the impinged area for each configuration;
- Comparison between the jets generated by both active and passive swirl generators;

The design principles of the heated thin-foil sensor, based on the convective heat transfer model and infrared radiation theory, are presented in chapter 2, together with an overview of the Quantitative Infrared Thermography (QIRT) measurement technique. chapter 3 provides the reconfiguration of the jet facility, including a detailed description of the heat flux sensor, nozzle and feeding line, and active and passive swirl generators. Subsequently, chapter 4 presents the main results of the QIRT campaign. After evaluating the Nusselt number maps, the analysis focuses on radial distributions and spatial uniformity, comparing the results with those obtained for a conventional axisymmetric jet and a passive swirled jet.

Chapter 2

Infrared thermography

2.1 Quantitative infrared thermography

Infrared (IR) thermography is currently one of the most widely adopted non intrusive techniques for the measurement of convective heat transfer in impinging jet configurations. In addition to its non intrusive nature, the use of infrared cameras offers several significant advantages, including full two-dimensional field measurement capability, high thermal sensitivity, and relatively fast temporal response, which make it particularly suitable for resolving spatially complex and highly localized heat transfer phenomena [24, 25, 26].

The method requires the presence of a thermal sensor, i.e. the surface where heat transfer takes place, and a thermal transducer, namely the infrared imaging system used to detect the emitted radiation. While different types of thermal sensors can be employed depending on the application, the core of the technique lies in the radiation detector integrated within the infrared camera, which enables the conversion of emitted infrared radiation into quantitative temperature information.

The working principle is based on the detection of infrared radiation naturally emitted by a surface as a function of its temperature. This radiation is collected by the camera optics and converted, through a calibrated response model, into spatially resolved temperature fields and, when required, temporally resolved temperature sequences. The accuracy of this conversion depends on a correct modelling of surface emissivity and environmental radiation contributions.

Once the surface temperature distribution is obtained, it is possible to determine the local convective heat transfer coefficient by applying an energy balance to the heated surface. From this, the corresponding Nusselt number distribution can be evaluated, allowing a detailed quantitative characterization of the heat transfer performance of the impinging jet.

2.2 Convective heat transfer model

The goal of the study is to estimate the convective heat flux between the jet flow and the impinged surface.
The heat flux q_c'' per unit area, meaning the energy which flows between a fluid and a surface as transferred heat per unit time and per unit surface, follows Newton's convection law:

$$q_c'' = h_c(T_w - T_{ref}) \tag{2.1}$$

Equation (2.1) correlates the heat flux with a difference between the wall temperature T_w and a reference temperature of the fluid T_{ref} through the convective heat transfer coefficient h_c. The reference temperature of the fluid depends on the stream conditions, which in the case of submerged impinging jets is considered to be the adiabatic wall temperature T_{aw}, representing the temperature at which the system is at thermal equilibrium and, as such, there is no heat transferred.

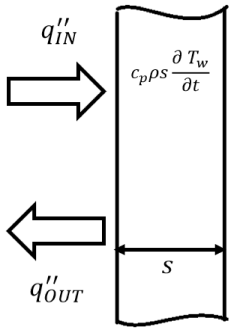


Figure 2.1: Local energy balance on the foil element of thickness s

The heated thin foil provides a method to evaluate heat transfer by locally applying the energy balance to the foil which can be represented by the sketch in figure 2.1 and described by the relation:

$$c_p \rho s \frac{\partial T_w}{\partial t} = q''_{IN} - q''_{OUT} \tag{2.2}$$

where c_p is the specific heat capacity, ρ is the density and s the thickness of the foil. Equation (2.2) states that the variation of energy in time per unit area is equal to the arithmetic sum of all of the heat fluxes flowing inward and outward of the foil element. To further characterize the physical model, two dimensionless numbers have to be evaluated, representing two important aspects of the heat transfer of the problem. First is the Biot number (Bi), that allows to evaluate if the assumption of a *thermally thin* material can be applied to the thin foil. Then is the Fourier number (Fo), characterizing the speed of heat diffusion and storage. These approximations of a physical model are validated through the evaluation of

the two dimensionless numbers, with the Biot number, representing the ratio of an object's internal thermal resistance to its external convective thermal resistance,

$$Bi = \frac{h_c s}{\kappa} \tag{2.3}$$

and the Fourier number, representing the ratio of the rate of conduction (or diffusion) to the rate of storage in a material, determining how quickly a body responds to thermal changes:

$$Fo = \frac{\alpha t_{char}}{s^2} \tag{2.4}$$

In equations (2.3) and (2.4), κ is the foil thermal conductivity, α it's thermal diffusivity and t_{char} a characteristic time of the phenomenon under exam. The assumption of a thermally thin material implies that the temperature is uniform across its thickness, while the comparison between the characteristic time scale of heat diffusion within the material and that of the flow provides an indication of the capability of the system to resolve temporal variations in the flow.
Including equation (2.1) in the energy balance, a formulation for the unknown convective heat transfer coefficient can be obtained:

$$h_c = \frac{q''_{IN} - q''_{OUT} - c_p \rho s \frac{\partial T_w}{\partial t}}{T_w - T_{aw}} \tag{2.5}$$

In this equation, h_c is expressed as a function of parameters that are all either known or measured. The results will then be expressed in form of dimensionless Nusselt number defined as:

$$Nu = \frac{h_c L}{\kappa_a} \tag{2.6}$$

where κ_a is the thermal conductivity of air and L is a characteristic length of the problem.

2.3 Infrared radiation measurements

Infrared radiation measurements are based on the detection of thermal radiation emitted by a body as a function of its temperature. The interpretation of these measurements requires an understanding of the fundamental principles of radiation heat transfer, as well as of the factors influencing the interaction between radiation and real surfaces. In this context, the role of surface properties and environmental conditions is crucial for accurately relating the detected signal to the actual temperature of the observed object.

2.3.1 Radiation heat transfer

The infrared camera sensing system uses radiation heat transfer to estimate the temperature of the body studied. Radiation heat transfer is an energy transport mechanism that occurs via electromagnetic waves. The radiation can interact with bodies by being absorbed or reflected by them or even passing through them. Energy conservation requires:

$$\alpha_r + \rho_r + \tau_r = 1 \tag{2.7}$$

denoting with α_r the radiation fraction being absorbed by the body, with ρ_r the fraction being reflected by it and with τ_r the fraction being transmitted through it. All surfaces at temperature greater than absolute zero $T > 0$ K emit thermal radiation, with the one emitting the greatest amount of energy being the *black body*. The total hemispherical emissive power of a black body follows the Stefan–Boltzmann law:

$$E_b = \sigma T^4 \tag{2.8}$$

while the spectral distribution of emitted radiation is according to Planck's law:

$$I_b(\lambda) = \frac{C_1}{\lambda^5(e^{\frac{C_2}{\lambda T}} - 1)} \tag{2.9}$$

In eqs (2.8), (2.9) $\sigma = 5.67 \times 10^{-8}$ W/m^{2}K^4 is the Stefan-Boltzmann constant, λ is the radiation wavelength , T the absolute black body temperature and C_1 and C_2 the first and the second universal radiation constants, respectively equal to 3.7418×10^{-16} W·m^2 and 1.4388×10^{-2} m·K.
Real objects almost never behave as a black body, and usually emit only a fraction of the total black body radiation I_b. By defining the emissivity coefficient as $\varepsilon(\lambda) = \frac{I(\lambda)}{I_b(\lambda)}$ we can rewrite equations (2.8) and (2.9) for real bodies as:

$$E = \varepsilon \sigma T^4 \tag{2.10}$$

$$I(\lambda) = \varepsilon(\lambda) \frac{C_1}{\lambda^5(e^{\frac{C_2}{\lambda T}} - 1)} \tag{2.11}$$

Bodies whose emissivity does not depend on wavelength are referred to as gray bodies. According to Kirchhoff's law, the spectral emissivity is equal to the spectral absorptivity $\alpha_r(\lambda)$, defined as the fraction of incident radiation at wavelength λ that is absorbed by the surface. For opaque (non transparent) materials, which are commonly used in infrared thermography, this leads to the relation:

$$\varepsilon(\lambda) + \rho_r(\lambda) = 1 \tag{2.12}$$

As a consequence, materials characterized by low emissivity, such as metals, not only emit a reduced amount of thermal radiation but also reflect a significant portion of the radiation originating from the surroundings. This reflective behavior can introduce substantial errors in temperature measurements. For this reason, such materials are generally avoided in infrared thermography. Whenever possible, the surface is typically coated with a thin layer of high emissivity paint in order to improve measurement accuracy.

2.3.2 Infrared cameras

The core of the IR camera system is the radiation detector. Detector technologies are mainly separated into two classes: thermal detectors, which are sensitive to the incident energy flux and quantum detectors, whose sensitivity depends on photon absorption.
Generally, the electromagnetic spectrum is divided in wavelength bands, among which the infrared spectrum is between 0.75 to 1000 µm. IR cameras detect emitted radiation in the middle infrared ($3 - 5$ µm) or long infrared ($8 - 12$ µm) bands and convert it to temperature using calibrated response curves [27, 24]. The total radiation I' detected by the camera depends on the emissivity of the surface and environmental conditions, and can be written as:

$$I' = \tau_r \varepsilon I_{b,obj} + \tau_r (1 - \varepsilon) I_{b,amb} + (1 - \tau_r) I_{b,atm} \tag{2.13}$$

where τ_r is the transmissivity of the atmosphere, $I_{b,obj}$, $I_{b,amb}$, $I_{b,atm}$ are the radiation intensities corresponding to a black body respectively at the object, ambient and atmosphere temperature. In equation (2.13), the term $\tau_r \varepsilon I_{b,obj}$ is the emission from the surface captured by the thermal detector, $\tau_r \, (1 - \varepsilon) I_{b,amb}$ is the reflected emission from ambient sources, and $(1 - \varepsilon)$ is the surface reflectivity (Tamb is assumed constant for all emitting surfaces of the half sphere seen from the object surface). The term $(1 - \tau_r) I_{b,atm}$ is the emission from the atmosphere, with $(1 - \tau_r)$ being he atmosphere emissivity.
The typical, simplified ($\tau_r = 1$), calibration function of an IR camera can be put in the form:

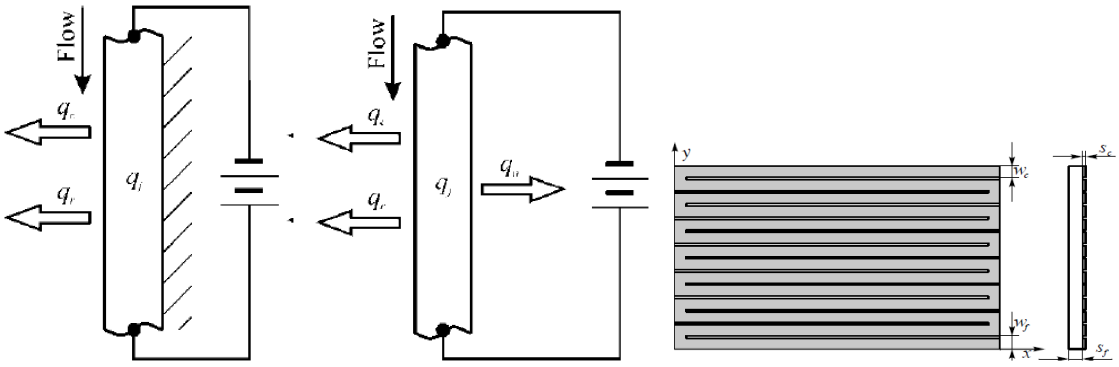
$$U_D = \varepsilon \frac{R}{e^{B/T_{obj}} - F} + (1 - \varepsilon) \frac{R}{e^{B/T_{amb}} - F} \tag{2.14}$$

where U_D is the detected signal, R is a function of integration time and wavelength, B is a function of wavelength alone, and F is a positive value very close to 1 [24]. The performance of an infrared imaging system is typically evaluated based on how much reliable and meaningful information it can deliver within a given time interval. This performance can be characterized by several parameters such as thermal sensitivity, also referred to as the equivalent random noise level; image

resolution, namely the number of independent measurement points composing the image; and intensity resolution, that is, the number of distinguishable intensity levels, which determines the ability to resolve small temperature differences and therefore defines the dynamic range.
The sensitivity of an infrared sensing system is generally quantified by the noise equivalent temperature difference (NETD). This parameter represents the temperature difference between two points in the image that produces a signal equal to the random background noise of the camera [28].

2.4 Heat flux sensors

The infrared camera acts as a thermal transducer by detecting the radiation emitted by a heated sensor placed in an appropriate position relative to the flow studied.



(a) adiabatic thin foil **(b)** diabatic thin foil **(c)** PCB

Figure 2.2: Examples of possible heat flux sensors, reproduced from [27]

One possible solution for a heat flux sensor is heated thin foil sensor, that consists of a thermally thin metallic foil, or a printed circuit board (PCB), steadily and uniformly heated by Joule effect. The PCB sensor (fig 2.2c) has the disadvantage that the current and thus the Joule heating must follow the printed path, leading to an anisotropic heating with a more difficult calculation for the tangential conduction along and across the tracks [27]. Foil heating can also be accomplished in a different way, for example, by a known steady radiation input to the foil [24]. It has to be noted however, that this kind of thermal input and it's spatial distribution is difficult to be precisely known, as material and ambient characteristics as well as view factors have to be taken into account. Another possible variation of thin-foil sensors is between diabatic and adiabatic sensors, as represented in figure 2.2b and 2.2a. A diabatic thin foil sensor exchanges heat through both its front and back surfaces, meaning that heat losses from the rear surface (by convection and

radiation) must be accounted for in the energy balance to accurately determine the convective heat transfer coefficient. In contrast, an adiabatic thin foil sensor is thermally insulated on its back surface, so all the supplied heat is assumed to leave through the front surface via convection and radiation, resulting in a simpler energy balance and reduced uncertainty.
The sensor designed and employed in the present work is a Joule heated diabatic metallic thin foil sensor. This configuration was chosen for its ability to provide uniform heating and because the diabatic arrangement allows the infrared camera to be positioned behind the sensor, thereby avoiding any disturbance to the impinging jet flow.
In this kind of sensor, the camera facing side is covered with a thin layer of black paint to maximize emissivity. To assume that all of the radiation heat flux is emitted on this side, the flow facing side is left reflective.

2.5 Data reduction

A more in depth analysis of equation (2.5) provides the tools to explicitly calculate the convective heat transfer coefficient h_c from the known and measured quantities. Considering all of the possible heat fluxes acting on the thin foil element, equation (2.5) can be rewritten as:

$$h_c = \frac{xs\frac{\partial T_w}{\partial t}}{T_w - T_{aw}} \tag{2.15}$$

where q''_{IN} and q''_{OUT} were substituted by the various heat fluxes actually contributing to the thermal balance. Each one of the terms is here analysed on his own.
The only term providing a positive increment of thermal energy is the Joule effect heat flux q''_j, evaluated as:

$$q''_j = \frac{I \cdot V}{A^*} \tag{2.16}$$

where I and V are respectively the current and voltage applied at the foil's contacts, and A^* is its surface area through which the current is discharged.
The terms contributing to the dissipation of the heat here considered are the tangential conduction losses, the radiation heat flux and the natural convection. Among these, q''_k is the term representing the thermal losses for tangential conduction. Assuming that the foil is thermally thin (condition that is verified in section 3.2), and considering x and y as the coordinates describing the foil's surface, it's distribution can be derived following [29] :

$$q''_k = q''_k(x,y) = -\underline{\nabla} \cdot [s(x,y)\underline{\underline{K}}(x,y) \cdot \underline{\nabla} T(x,y)] \tag{2.17}$$

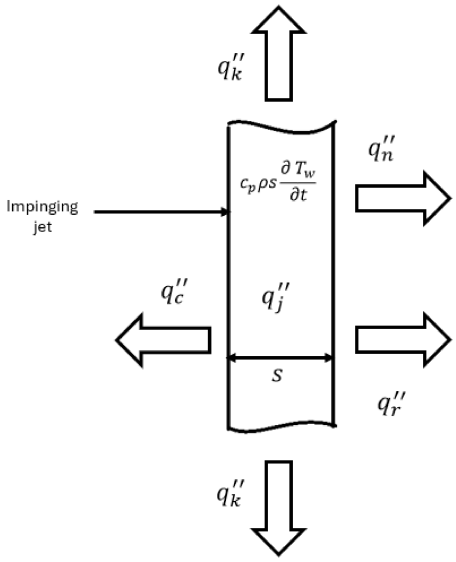


Figure 2.3: Heat fluxes contributing to the local energy balance of the foil element

Where $\underline{\underline{K}}$ is the local foil thermal conductivity tensor and s is the sensor thickness. For an isotropic, plane, metallic foil sensor, it is possible to write:

$$q_k'' = \kappa_f \cdot s \cdot \nabla^2 T_w \tag{2.18}$$

where κ_f is the foil thermal conductivity, uniform throughout the surface. Since the sensor is composed by the metallic foil and a thin layer of paint, the different thermal conductivities of each material must be accounted for. As such, the thermal conductivity κ_p and thickness s_p of the paint are included in equation (2.18) and it becomes:

$$q_k'' = (\kappa_f s_f + \kappa_p s_p) \cdot \nabla^2 T_w \tag{2.19}$$

The radiation heat flux q_r'' that is lost from the foil to the environment is then estimated following Stefan-Boltzmann law:

$$q_r'' = \sigma \varepsilon (T_w^4 - T_{amb}^4) \tag{2.20}$$

assuming the surroundings behave as a black body at ambient temperature T_{amb}, with σ being the Stefan-Boltzmann constant and ε the emissivity of the surface. The natural convection q_n'' is ceded from the back of the sensor to the surrounding air, and also follows Newtons' convection law:

$$q_n'' = h_n (T_w - T_{amb}) \tag{2.21}$$

with h_n being the natural convective heat transfer coefficient.

All of the above mentioned contributions to the energy balance are expressed through known quantities such as input parameters, material properties, and physical constants. Therefore, it is now possible to evaluate h_c from equation (2.15) with the sole measure of the distribution of T_w and T_{aw} with a heat flux sensor as explained in section 2.4. From this can be derived the Nusselt number distributions. The uncertainty of the evaluated Nusselt number is estimated following the methodology described in [30], where the uncertainty of each variable considered is taken into account to obtain an estimate of the uncertainty of Nu. This process is described in detail in appendix A

Chapter 3

Methodology

The experiments were carried out in the Modesto Panetti Laboratory at Politecnico di Torino. Having introduced the methodology and technique applied in this work, this section provides further details about the actual instrumentation and procedures implemented. The setup was adapted from previous experimental campaigns in the same jet facility [23, 22] to fit the needs of thermographic measurements.

3.1 Jet facility

The jet facility remains mostly unchanged from the works conducted in the previous Master Theses [23, 22], with a few key modifications that suit the requirements of the experimental campaign. The convergent nozzle shape, designed based on the Vitoshinski nozzle [31], as given by equation (3.1), was developed during a previous work [22], and continued to be employed.

$$r(x) = \frac{R_e}{\sqrt{1 - \left[1 - \left(\frac{R_e}{R_i}\right)^2\right] \frac{\left(1 - \frac{x^2}{L^2}\right)^2}{\left(1 + \frac{x^2}{3L^2}\right)^3}}} \tag{3.1}$$

This equation provides the radius value r along the nozzle axis x, given an inlet and outlet radius R_i, R_e, and a total length of the nozzle L.
Additionally, it was also emploiyed a 3D-Printed support designed to fit different nozzle inserts such as the passive and active swirl generators. The nozzle was fitted with static pressure taps at both the inlet and outlet, with the pressure drop correlated with the axial exit velocity along the jet centerline for the round jet through a Pitot measurement campaign (Appendix B). The static pressure ports were also used to evaluate the resistance to the flow imposed by a given swirler.

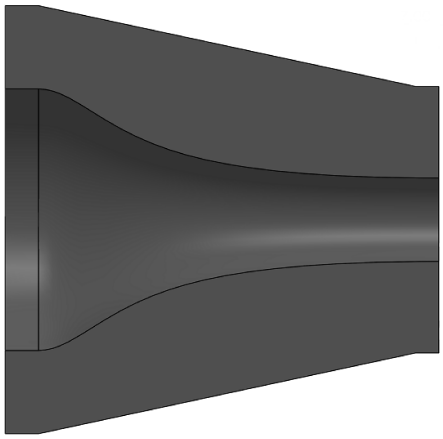


Figure 3.1: Section view of the Vitoshinsky nozzle

Compressed and filtered air is delivered through a pneumatic line shown in figure 3.2 and regulated by a system of two valves, consisting of one valve for coarse adjustment and a second valve for fine pressure control.

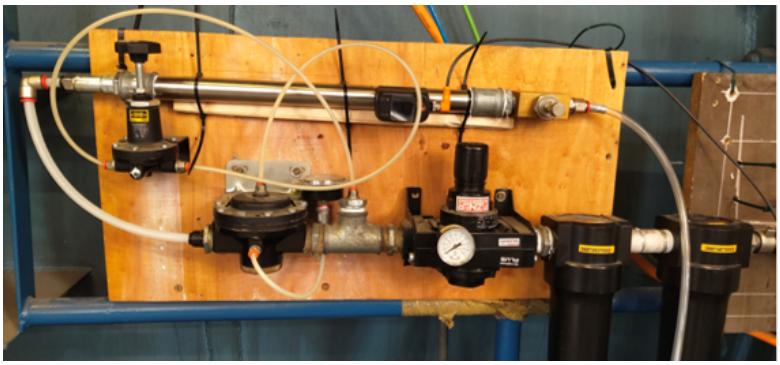


Figure 3.2: Section of the feeding line including air filters, fine and coarse pressure regulators and mass flow meter

The feeding line was equipped with a flowmeter that allowed the measurements to be performed under fixed mass flow conditions. Between the flowmeter and the jet facility was also implemented the possibility to add to the line a Laskin nozzle, a device that works as an atomizer and fills the air with nebulised seeding particles. This enables the ability to acquire some qualitative images of the stream conditions and flow structures as further described in appendix C.
The jet assembly with its supporting structure was mounted on a linear rail system to allow adjustment of the nozzle to plate spacing. This configuration enables variation of the impingement distance, consenting measurements over a set of different conditions.

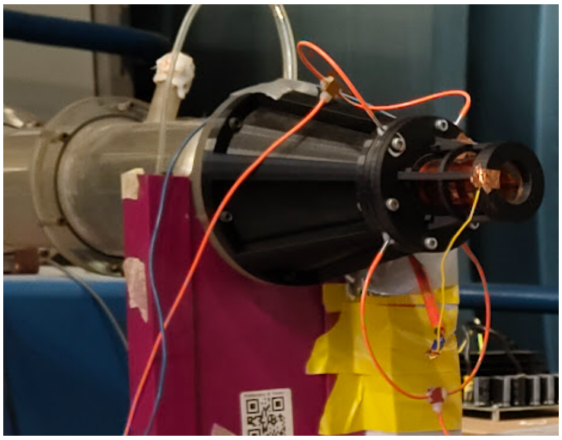


Figure 3.3: Jet nozzle with plasma swirler mounted

3.2 Heat transfer measurements

The IR Thermography setup consists of a Joule-heated thin-foil heat flux sensor and a thermal camera (Infratec ImageIR® 6300Z). A sketch of the experimental setup is reported in figure 3.4

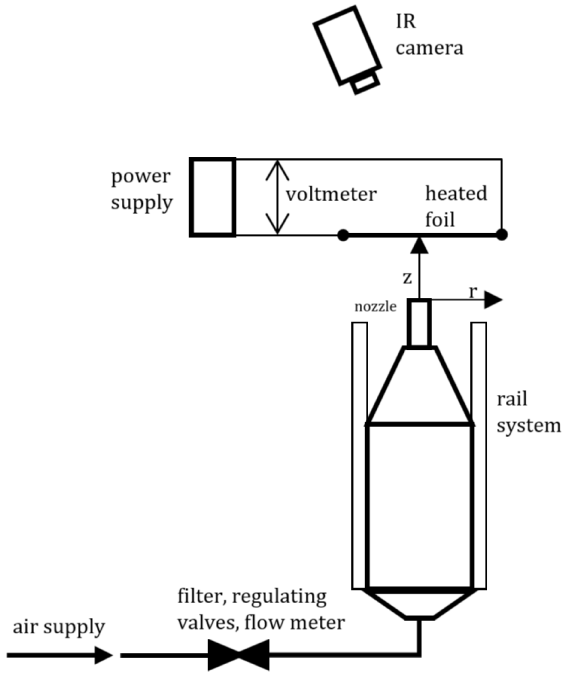


Figure 3.4: Sketch of the thermographic experimental setup

3.2.1 Heat flux sensor

A heated thin foil sensor was designed and mounted vertically in front of the jet nozzle to serve both as a heat flux sensor and as the impinged surface. The sensor was built in a 300×300 mm wooden frame, fitting a thin foil with a sensing area of width 203 mm and height 290 mm. The frame was mounted on a fixed structure aligned with the jet axis. The foil has a thickness of 20 µm and is made of a CrNi-Steel alloy, with properties reported in Table 3.1 .

Table 3.1: Heat transfer characteristics of the materials composing the sensor

Foil properties			
Density	ρ_f	7900 ± 50	kg/m^3
Heat Capacity	$c_{p,f}$	500 ± 5	J/(kg K)
Thermal conductivity	κ_f	17 ± 2	W/(m K)
Thermal diffusivity	α_f	$(4.30 \pm 0.5) \cdot 10^{-6}$	m^2/s
Paint properties			
Density	ρ_p	1300 ± 50	kg/m^3
Heat Capacity	$c_{p,p}$	5000 ± 5	J/(kg K)
Thermal conductivity	κ_p	1.4 ± 0.1	W/(m K)
Thermal diffusivity	α_p	$(2.15 \pm 0.5) \cdot 10^{-6}$	m^2/s
Emissivity	ε	0.95	$\sim$

The thin foil is covered with a high emissivity coating consisting in a layer of black paint on the camera facing side. Properties of the paint are also reported in Table 3.1.

On the back of the frame are mounted four threaded rods, holding two pairs of copper bars with 10×10 mm square section. Each pair clamps one free end of the foil to hold it in position, applying tension by means of four springs mounted coaxially to the threaded rods. The foil is taut between two steel bars covered with PVC tubes to insulate them electrically. The thin foil is heated through Joule effect, with the copper bars working as electrical contacts. The uniform thickness of the foil ensures a constant heat flux distribution. Infrared measurements of the heated surface confirmed that the resulting temperature field is nearly uniform in space. Joule heating is applied by connecting a DC power supply to one end of the copper electrodes. Due to the significantly higher electrical resistance of the steel foil compared to that of the copper, together with its much smaller thickness, the electrical potential drop across the copper blocks is negligible relative to that across the foil. As a consequence, the copper electrodes can be assumed to be at uniform potential, which guarantees a uniform distribution of both voltage and current along the vertical direction.

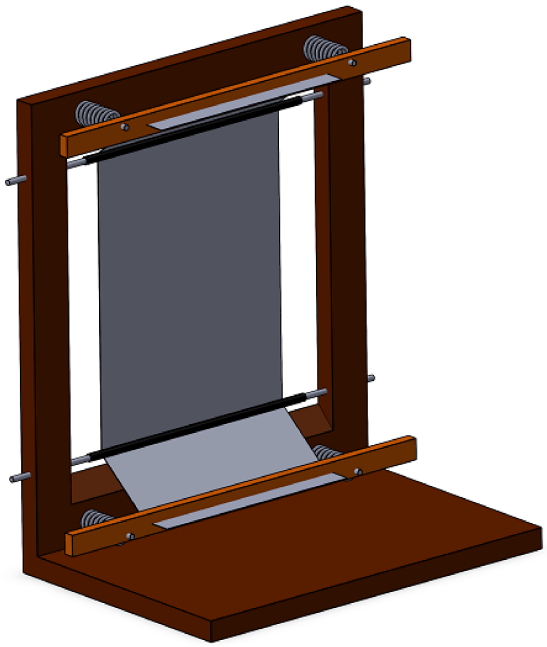


Figure 3.5: 3D CAD model of the heat flux sensor

A BK Precision power supply BK1693 is used to supply a steady current to the foil in order to achieve the Joule heating. The applied current is between 22 and 29 Amperes, depending on the test case and expected Nusselt number. The choice of the input electrical power is made to ensure a difference between T_w and T_{aw} sufficiently large for an accurate and reliable heat transfer measurement. At the opposite end of the copper electrodes is connected a multimeter that provides the voltage measure necessary to evaluate the energy dissipated via Joule effect. This value is found to be between 2.4 and 3.2 Volts and is reported, along with other sensor properties, in table 3.2.

Table 3.2: Geometrical and electrical parameters of the heated thin-foil sensor

Quantity	**Symbol**	**Value**	**Units**
Thickness	s_f	$2 \cdot 10^{-5}$	m
Height	H	0.290	m
Width	W	0.203	m
Sensing area	A	0.059	m^2
Joule area	A^*	0.082	m^2
Voltage	V	$2.4 - 3.2$	V
Current	I	$22 - 29$	A

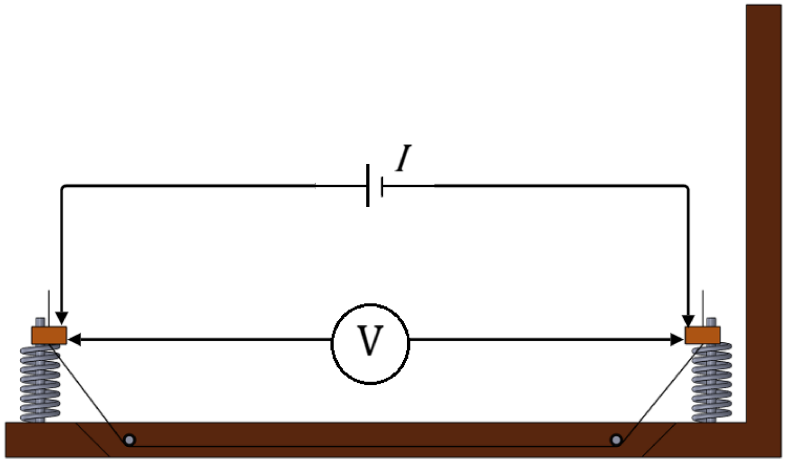


Figure 3.6: Electrical configuration of the Joule heating system

Knowing the material properties and geometry of the foil, it is possible to estimate the dimensionless Biot and Fourier numbers, validating the thermally thin assumption and the range of frequencies that the setup is able to resolve. The assumption of a thermally thin material implies that the temperature is uniform across its thickness, so that the temperature on the flow-facing side is equal to that on the opposite face. This condition is satisfied when the Biot number is much smaller than unity. If this condition is verified, it is safe to assume that the temperature measured on the side facing the IR camera correctly estimates the values considered in the physical model. Moreover, the comparison between the characteristic time scale of heat diffusion within the material and that of the flow provides an indication of the ability of the camera system to correctly detect flow fluctuations. A Fourier number much greater than 1 ensures that the thermal response of the material is sufficiently fast to resolve temporal variations in the flow. The Biot number can be estimated as:

$$Bi = \left(\frac{s_f}{\kappa_f} + \frac{s_p}{\kappa_p} \right) h_c = 8.32 \times 10^{-6} \cdot h_c \tag{3.2}$$

Assuming from literature an expected h_c of roughly 10^2 W/m^{2}K, equation (2.3) gives a Biot number well under unity, validating the thermally thin foil assumption. Similarly, it can be estimated the range of frequency that the sensing apparatus can resolve. Accounting for the impact on the thermal behaviour of the high emissivity coating, the equivalent diffusivity is:

$$\alpha_{eq} = \frac{k_{eq}}{(\rho c)_{eq}} = 2.003 \times 10^{-6} \tag{3.3}$$

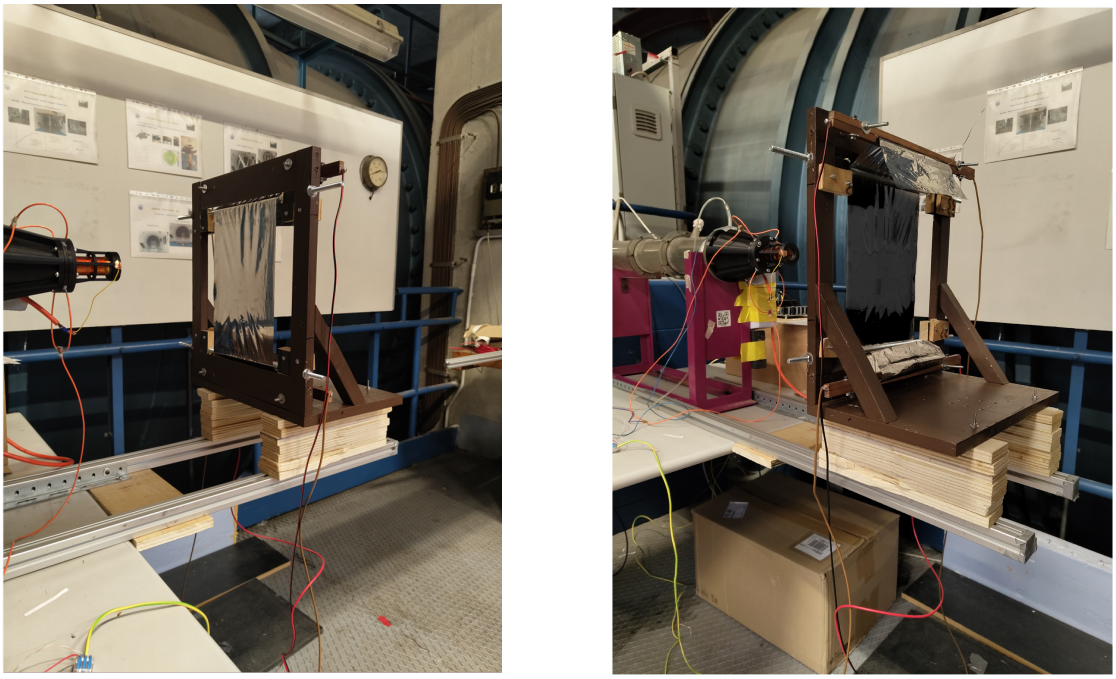
where:

$$k_{eq} = \frac{s_f + s_p}{\frac{s_f}{k_f} + \frac{s_p}{k_p}} \tag{3.4}$$

$$(\rho c)_{eq} = \frac{(\rho c)_f s_f + (\rho c)_p s_p}{s_f + s_p} \tag{3.5}$$

The Fourier number evaluated for the sensor composed of the thin metallic foil and the coating layer is then:

$$Fo = \frac{\alpha_{eq}}{(s_p + s_f)^2} t_{char} = 2.225 \times 10^3 \cdot t_{char} \tag{3.6}$$



(a) Jet facing side **(b)** Camera facing side

Figure 3.7: Heated thin foil heat flux sensor

The phenomenon studied can be described as a composition of a mean flow and a fluctuating turbulent component. The expected frequency of the turbulent fluctuations at this scale is in the 10^3 to 10^4 Hz range [32]. This implies that the temporal fluctuations, with a characteristic time of $10^{-3} - 10^{-4}$ seconds, cannot be resolved, as the corresponding Fourier number becomes smaller than unity. Therefore, this study focuses on analyzing the mean flow, evaluating a steady state condition.

3.2.2 Infrared camera

An Infrared Camera is employed as a temperature transducer to measure the temperature on the outside of the sensor. The temperature measurements in this study were performed using an Infratec ImageIR® 6300Z IR camera, featuring a spatial resolution of 640×512 pixels. The camera provides a noise equivalent temperature difference (NETD) of 0.03 K at 30 °C, with a calibration accuracy of ± 2 K. The camera was placed at ~ 40 cm from the sensor, with a slight angle to avoid capturing the reflection of it's own radiation. The camera zoom and focus were adjusted in order to capture a rectangular region of dimensions 206×165 mm, leading to a spatial resolution of 3.105 px/mm. To minimize environment noise, the entire setup was shielded from external radiation with black curtains.

3.3 Swirl generators

This work aims to study the effects on heat transfer of an active swirl generator. A multichannel helical passive swirler provides the benchmark against which these effects are compared. This section briefly describes their characteristics.

3.3.1 Passive swirlers

The passive method to induce a swirl motion in the flow is a 4-channel helical insert, with guided vanes based on the geometry proposed in [3]. An empirical equation presented in [33] was used to relate the swirl number of the flow S with the geometrical characteristics of the helical insert:

$$S = \frac{2}{3} \frac{\left[1 - \left(\frac{d}{D}\right)^3\right]}{\left[1 - \left(\frac{d}{D}\right)^2\right]} \tan\theta \tag{3.7}$$

where D is the internal nozzle diameter of the injector, d represents the hub diameter, and θ is the swirling angle. Having fixed the nozzle and hub diameters, it is possible to express the angle θ and the corresponding helical pitch h as a function of the desired swirl number:

$$\tan\theta = \frac{3}{2} \frac{\left[1 - \left(\frac{d}{D}\right)^2\right]}{\left[1 - \left(\frac{d}{D}\right)^3\right]} S \tag{3.8}$$

$$h = \frac{D}{\tan\theta} \tag{3.9}$$

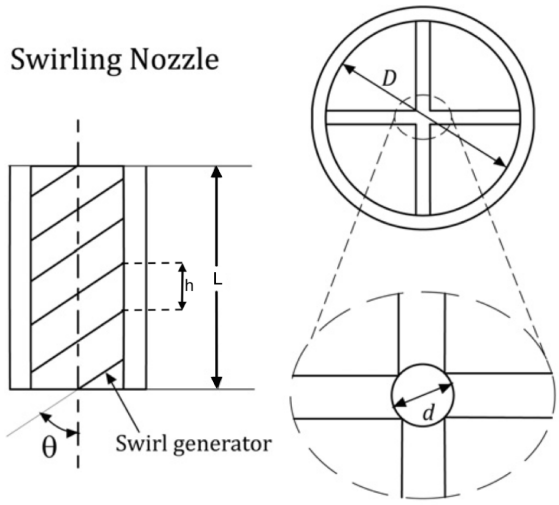


Figure 3.8: Sketch of the passive multichannel helical swirler, reproduced from [3]

One complete helical revolution corresponds to an axial increase of $4h$. Therefore, the number of revolutions R within a fixed length L is given by:

$$R = \frac{L}{4h} \tag{3.10}$$

Based on the results of the previous experimental campaigns [22, 23], only one passive swirler is employed, with a low swirl number of $S = 0.1$. The geometrical characteristics of such swirler are reported in Table 3.3

Table 3.3: Geometric parameters of multichannel passive swirl generator

Quantity	**Symbol**	**Value**	**Units**
Swirl number	S	0.1	$\sim$
Length	L	70	mm
Nozzle diameter	D	25	mm
Hub diameter	d	2.83	mm
Swirling angle	θ	8.43	deg
Revolutions	R	0.10381	$\sim$

With this known geometry, the insert was designed with the aid of a CAD platform using SolidWorks 3D modeling software and manufactured with a BambuLab P1S 3D Printer.

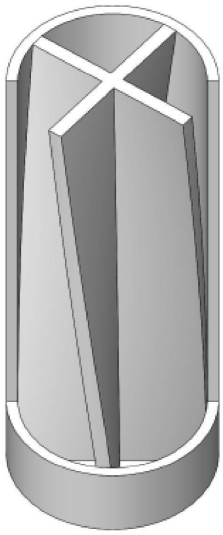


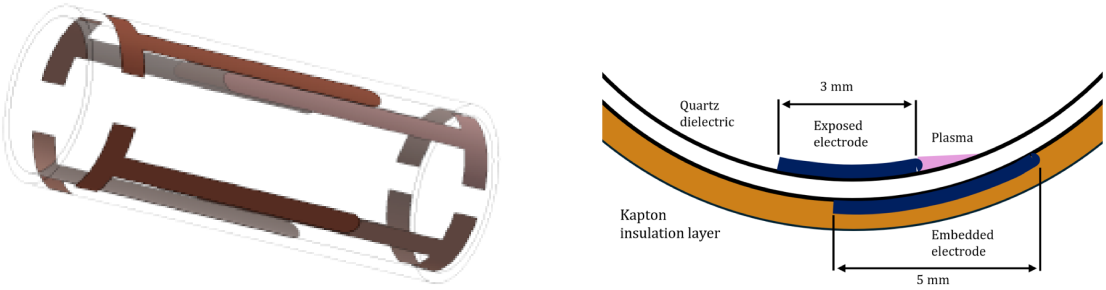
Figure 3.9: 3D CAD model of the passive multichannel helical insert, reproduced from [22]

3.3.2 Active swirlers

For the active swirl generator, the swirler developed in [23] was employed, which was designed according to the methodology proposed in [11]. Four pairs of electrodes were positioned along the axial direction of injector and evenly spaced through it's circumference, composing four DBD Plasma Actuators connected in parallel. The injector is a quartz tube of 1.5 mm thickness and 70 mm length and it's walls also serve as the dielectric barrier. Quartz was chosen as the tube material due to its enhanced dielectric properties and resistance to electric discharges. Each electrode consists of a 0.35 mm thick copper foil tape. The wider electrode, measuring 5 mm in width and 50 mm in length, was placed inside the injector and exposed to the air. The narrower electrode, 3 mm wide and 45 mm long, was positioned externally and insulated with ten layers of Kapton tape. The swirl generator is actuated according to configurations B and C identified in the previous work [23], with peak-to-peak voltage V_{pp}, actuating frequency f and swirl number reported in Table 3.4

Table 3.4: Electrical and swirl parameters of the active swirl generator

Case	V_{pp} [kV]	f [kHz]	S
B	16	19	0.1009
C	19	19	0.1288



(a) 3D CAD model, reproduced from [23]

(b) Sketch of the electrode geometry

Figure 3.10: Active swirl generator

3.4 Electrical configuration

The electrical configuration involved the simultaneous activation of all DBD-PAs at the specified peak-to-peak voltage levels. The encapsulated electrodes were connected to ground, while the exposed electrodes were connected to the high voltage generator shown in figure 3.11 (GBS Elektronik GmbH Minipuls 4).

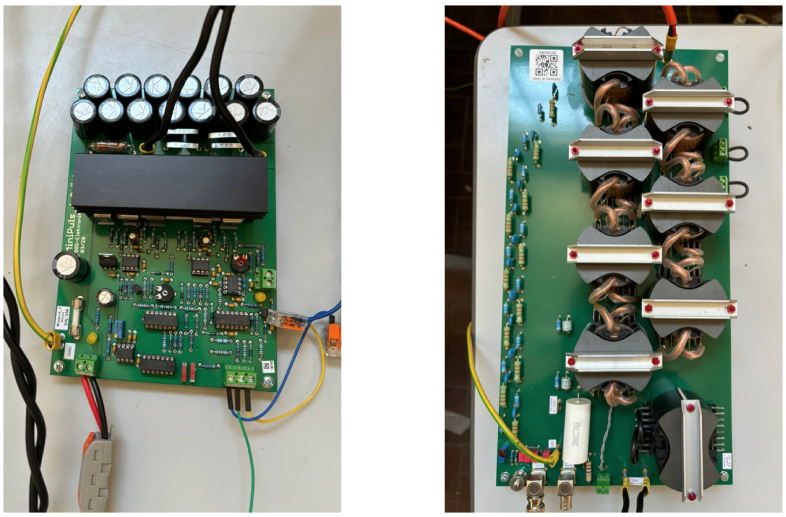


Figure 3.11: Components of the GBS Elektronik GmbH Minipuls 4: bridge converter (left) and transformer cascade (right)

This configuration was chosen to avoid the risk of discharge to nearby metallic components such as bolts and screws. The high voltage generator is a device based on a full-bridge converter that produces a low voltage square waveform, which is subsequently transformed and filtered by a transformer cascade to obtain a high voltage, sine-like waveform output.

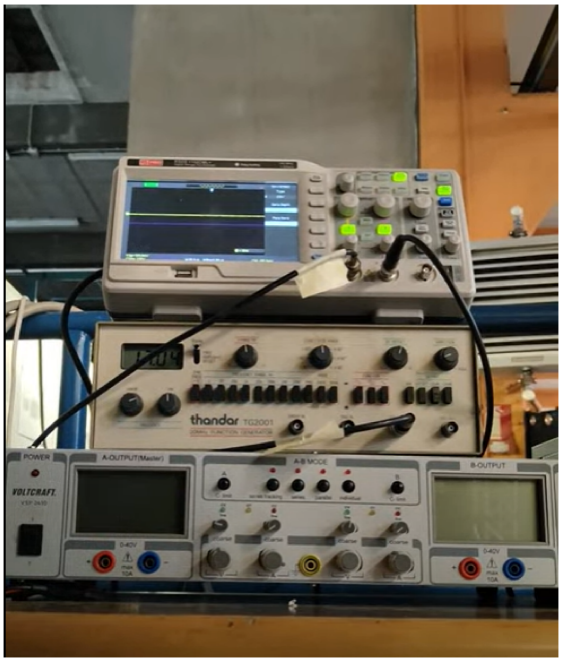


Figure 3.12: Elements of the experimental setup, from top to bottom: oscilloscope, function generator, power supply

The input power stage of the system is supplied by a DC power supply (Voltcraft VSP-2410), which provides the required regulated voltage to the bridge converter. The DC to AC conversion is controlled through a function generator (Thandar TG2001), which defines the excitation frequency and waveform characteristics of the system. The resulting high voltage AC signal produced by the transformer cascade is continuously monitored using an oscilloscope (RS PRO RSDS1102CML+), allowing verification of signal stability and operating conditions during experiments.

3.5 Data analysis and reduction

The heated thin foil sensor is used to evaluate both the wall temperature and the adiabatic wall temperature of the flow. This achieved by acquiring two distinct thermal images under different operating conditions. A first acquisition, called the *cold image*, is performed without supplying heating power to the sensor and is used to determine T_{aw}. This corresponds to the temperature distribution of the sensor solely influenced by the flow. A second acquisition, referred to as the *hot image*, is obtained with the heated sensor and is used to map T_w, representing the wall temperature under imposed heat flux conditions. For each analyzed case, at least three repeated tests of 500 snapshots were acquired both for the cold and hot

images at a frequency of 20 Hz, giving a sample time of 25 seconds. The images were acquired after a buffer time of 10-12 minutes given for the phenomenon to stabilize at steady state. Data acquisition was performed with the proprietary Infratec camera software, while the exported data was processed with a custom developed MATLAB code.
As already discussed in section 3.2.1, the sensor does not allow to resolve temperature fluctuation with frequency higher than $10^{-}3$ Hz as the corresponding Fourier number becomes smaller than unity. For this reasons, due to the thermal inertia of the foil and the averaging process applied to the acquired images, the present measurements must be considered as time averaged, meaning that temperature fluctuations associated with turbulence are not resolved. Before averaging the 500 acquired images, a filtering procedure is applied to identify and remove potential outlier temperature values arising from spurious measurements of the infrared camera. From these averaged temperature maps the data reduction explained in detail in section 2.5 is performed, obtaining a Nusselt map distribution for each case analyzed.
From these distributions, two ways of presenting the data are implemented. The first option is to present the Nusselt reduced data as surface averaged Nusselt number Nu and surface standard deviation percentage of Nusselt number σ_{Nu} as a function of the radial coordinate r:

$$\overline{Nu}(r) = \frac{1}{\pi r^2} \int_0^r \int_0^{2\pi} Nu(\rho, \theta) \rho d\theta d\rho \tag{3.11}$$

$$\sigma_{Nu} = \frac{\frac{1}{\pi r^2} \int_0^r \int_0^{2\pi} \left(Nu(\rho, \theta) - \overline{Nu}(r) \right)^2 \rho d\theta d\rho}{\overline{Nu}(r)} \cdot 100 \tag{3.12}$$

The second way involves the azimuthal average of the Nusselt number over a circumference of radius r and it's standard deviation:

$$\langle Nu \rangle_\theta = \frac{1}{\pi r} \int_0^{2\pi} Nu(r, \theta) r d\theta \tag{3.13}$$

$$\sigma_{\langle Nu \rangle} = \frac{1}{\pi r} \int_0^{2\pi} \left(Nu(r, \theta) - \langle Nu \rangle_\theta \right)^2 r d\theta \tag{3.14}$$

Nu maps and radial distributions of surface and azimuthal average Nu and σ_{Nu} are used to quantify the convective heat transfer rate and uniformity and to deduce the flow field structure.
For each case studied, the measurement process was performed three separate times. The uncertainty propagation is applied to the gathered data as shown in Appendix A, using the parameter uncertainties reported in Table 3.5. The uncertainty on the Nusselt number is found to be less than $\pm 3\%$. A measurement set is considered

Table 3.5: Uncertainty contributions for Nusselt number calculation

Parameter	**Uncertainty**	**Parameter**	**Uncertainty**
T_w	0.1 K	W	0.001 m
T_{aw}	0.1 K	ε	0.2
T_{amb}	0.1 K	κ_a	1%
V	0.5%	κ_f	2 W/(m K)
I	0.5%	κ_p	0.1 W/(m K)
D	0.0001 m	s_f	5%
H	0.001 m	s_p	5%

acceptable if at least two repetitions fall within the corresponding uncertainty bounds. Any measurement not in accordance with this condition is discarded.
To assess the compliance of this criterion, two strategies are adopted. The first is an evaluation over the radial distribution calculated for each measurement against the uncertainty bounds for which an example is provided in figure 3.13. The second strategy is a point-to-point comparison of each map against the mean of all the tests measured (figure 3.14). The final reported distributions are obtained by averaging the results of the compliant measurements.

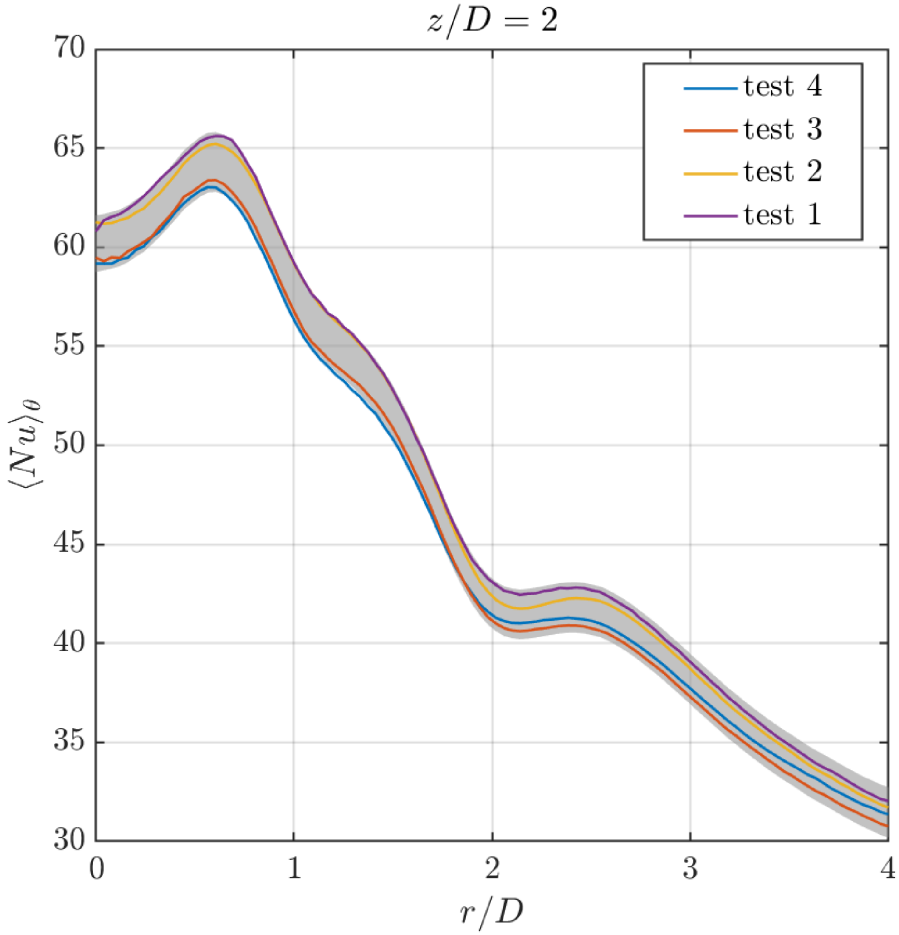


Figure 3.13: Radial distributions Nu for each repeated test compared with the δNu tolerance

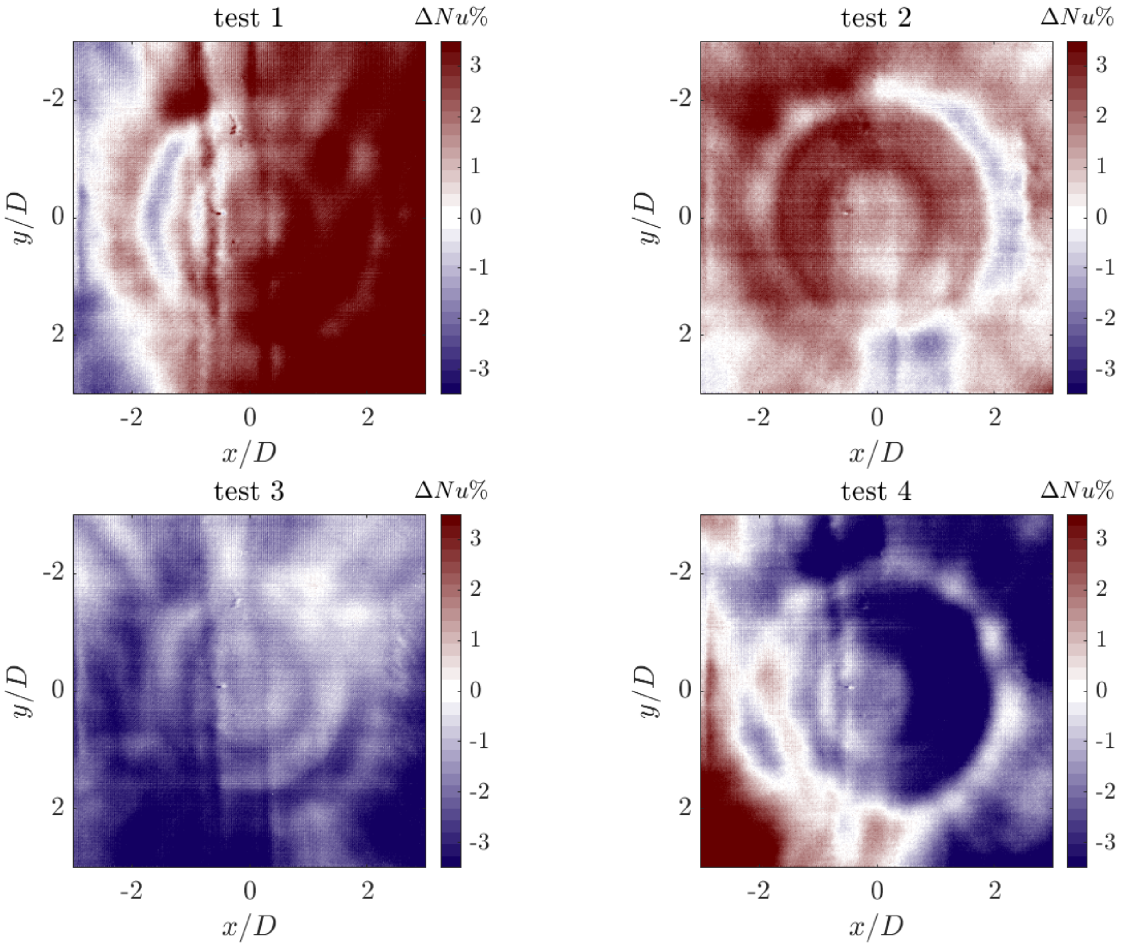


Figure 3.14: Surface distribution of the percentage Nu variation from the mean across the repeated tests

Chapter 4

Results

This chapter provides the main results concerning the thermographic campaign, distinguishing between a first set of measurements to asses the qualities of the setup, and the actual experimental campaign focused on DBD-PA swirl generators. The first investigation was conducted on a simple circular, non-swirling, impinging jet, choosing two velocity conditions, characterized by a Reynolds number of 4400 and 16000. These values were chosen to be comparable with reviewed literature data [34, 35, 36]. The flow conditions were controlled by fixing a defined mass flow, related to the bulk Reynolds number as:

$$\dot{m} = \frac{1}{4}\pi\mu DRe \tag{4.1}$$

Tests were performed at nozzle-to-plate distances $z/D = [0.5,\ 1,\ 1.5,\ 2,\ 4,\ 6,\ 8]$. For the sake of clarity, the results are mostly reported only for distances $z/D = [0.5,\ 2,\ 8]$ representing the low, mid, and high end of the investigated range. The main study was then conducted on the plasma based active swirler and the helical passive swirler, both at Reynolds $Re = 4400$, in order to maintain comparable conditions to those of the round jet. All tested conditions are reported in table 4.1.

Table 4.1: Flow and actuating conditions for each testcase

Case	Reynolds	Additional Conditions
Round Jet Low Re	4400	$\sim$
Round Jet High Re	16000	$\sim$
Passive Swirler	4400	$S = 0.1,\ \theta = 8.43°$
DBD-PA swirler B	4400	$V_{pp} = 16$ kV, $f = 19$ kHz
DBD-PA swirler C	4400	$V_{pp} = 19$ kV, $f = 19$ kHz

4.1 Methodology validation

The heat transfer maps for the non-swirling circular impinging jet in Figures 4.1, 4.2 exhibit the characteristic features of axisymmetric impinging flows reported in the literature [34, 35]. For the lower Reynolds number case ($Re = 4400$), at short

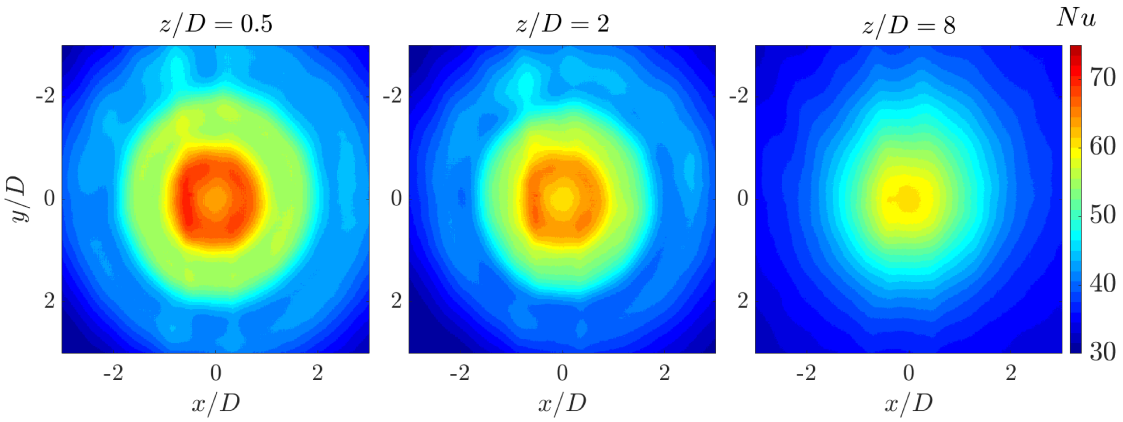


Figure 4.1: Heat transfer maps for Circular Jet at $Re = 4400$

impinging distances the Nusselt number distribution shows a local minimum at the stagnation point, surrounded by an annular region of maximum heat transfer located around $r/D = 0.5$, which is associated with the zone where the highest radial acceleration between the plate and the nozzle lip occurs [1]. The overall intensity of heat transfer decreases as the nozzle-to-plate spacing increases, up to $z/D = 2$, which is the largest distance at which the ring shaped structure remains clearly identifiable. There is also an outer region with a local Nu maximum around $r/D = 1.5$ that is shown more clearly by the azimuthally averaged Nusselt radial profiles. This region is typically attributed to the enhancement of heat transfer induced by entrainment associated with the development of vortex rings in the shear layer. These vortex structures interact with the incoming flow, promoting local flow separation followed by turbulent reattachment downstream, thus increasing convective heat transfer [3]. Similar flow structures are also observed for the higher Reynolds number case ($Re = 16000$), with a more pronounced secondary annular region and the corresponding peak shifted to approximately $r/D = 2$. The influence of the Reynolds number on the heat transfer appears as an increase in the Nusselt number over the entire impinged area. The shift of the secondary peak and overall heat transfer increase are well documented effects of the jet's Reynolds number [5, 37]. At greater distances, the radial profiles show a bell-shaped curve, with the corresponding Nu maps appearing with a pronounced peak at the stagnation point and a gradual decay in the radial direction.

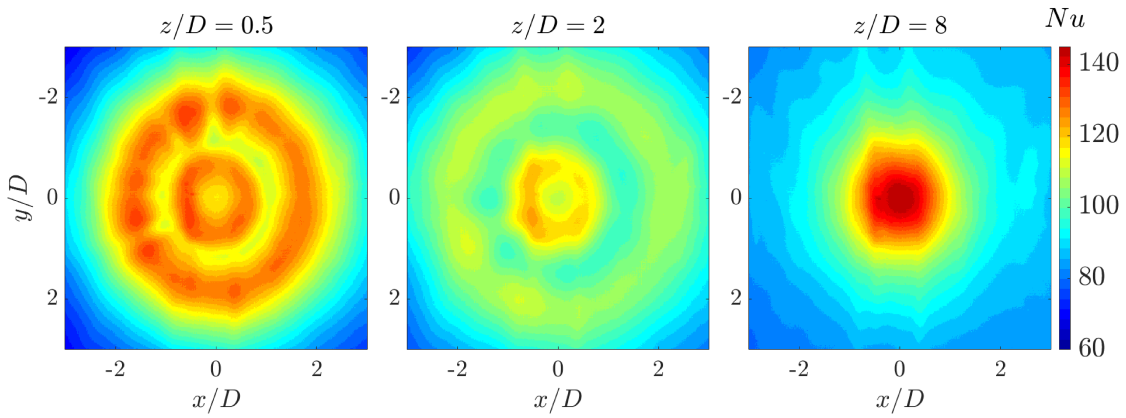


Figure 4.2: Heat transfer maps for Circular Jet at $Re = 16000$

Radial profiles in Figure 4.3 show that Nu has little dependence on the nozzle-to-plate distance in regions for which r/D is higher than 3, while the inner peak decreases as z/D increases from 0.5 to 2, and subsequently increases for larger impinging distances. Considering the range of z/D spacings investigated, only the lower Reynolds number case exhibits a further decrease beyond $z/D = 6$.
All these results are in good accordance with literature findings.

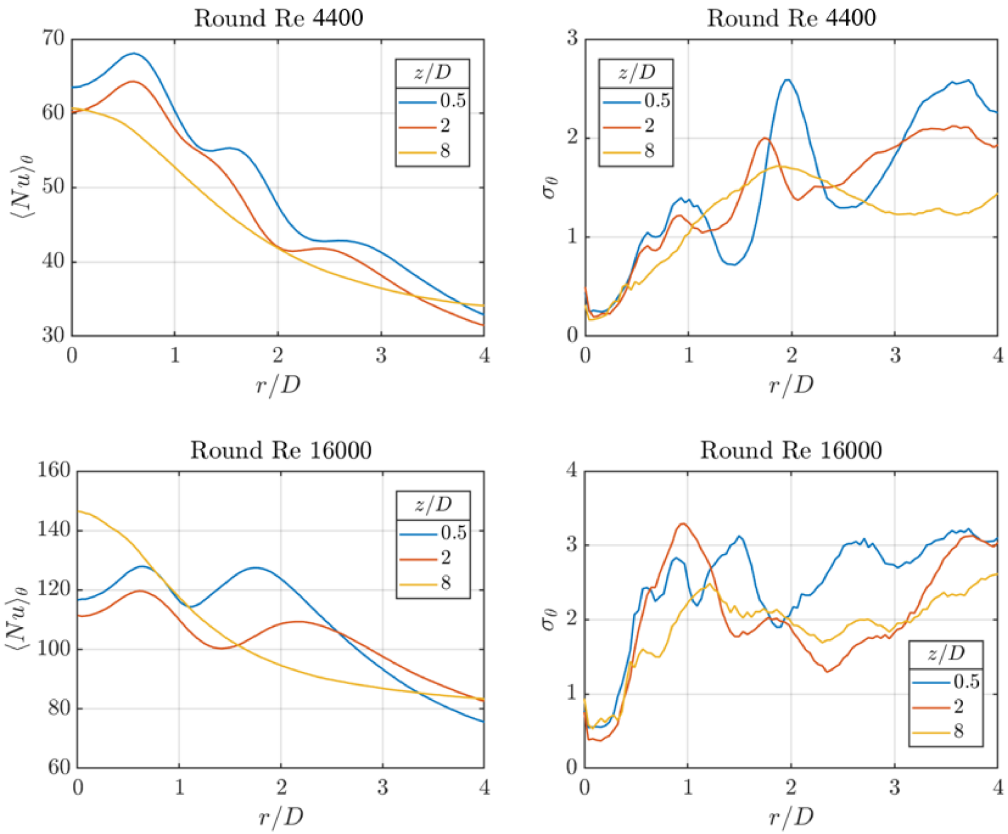


Figure 4.3: Azimuthally averaged Nusselt and standard deviation radial profiles for Round Jet at $Re = 4400$ and $Re = 16000$

4.2 Active vs passive swirlers

This section provides the comparative results of the swirling impinging jet with swirl generated by passive and active methods, under the test conditions summarized in Table 4.1. The two operating conditions of the DBD-PA produce very similar results; therefore, where appropriate, only Case B is reported.

4.2.1 Heat transfer maps

In Figure 4.4 are shown the heat transfer results for the helical multichannel swirling jet. The obtained distributions are in good agreement with the findings of Ianiro and Cardone, [3], who investigated the same geometry, with a slightly higher swirl number.
The Nu maps show four distinct stagnation zones for short impinging distances, clearly distinguishable up to $z/D = 2$. This phenomenon is due to the presence

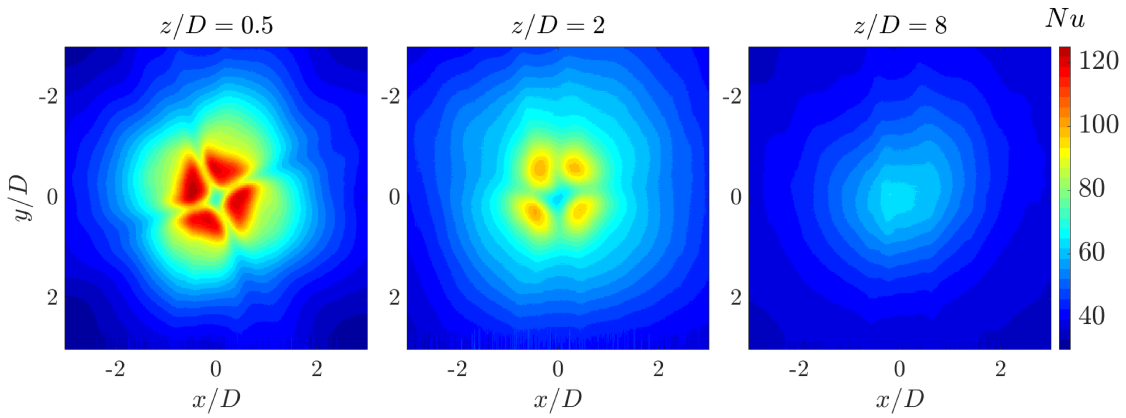


Figure 4.4: Heat transfer maps for Multichannel Passive swirler at $Re = 4400$

of the four channels within the insert that split the flow into separate jets. At larger nozzle-to-plate distances, the individual jets tend to merge into a single impingement region. In contrast to the circular impinging jet, the maximum Nusselt number values are observed at the smallest considered distance, followed by a monotonic decrease as the nozzle-to-plate spacing increases. It is relevant also to notice that the peak values of the Nusselt number are higher than those of the round jet, up to 75% at $z/D = 0.5$ and 45% at $z/D = 2$. The characteristic two-ring structure of the circular jet disappears, giving way to a four lobe structure around the stagnation zones.

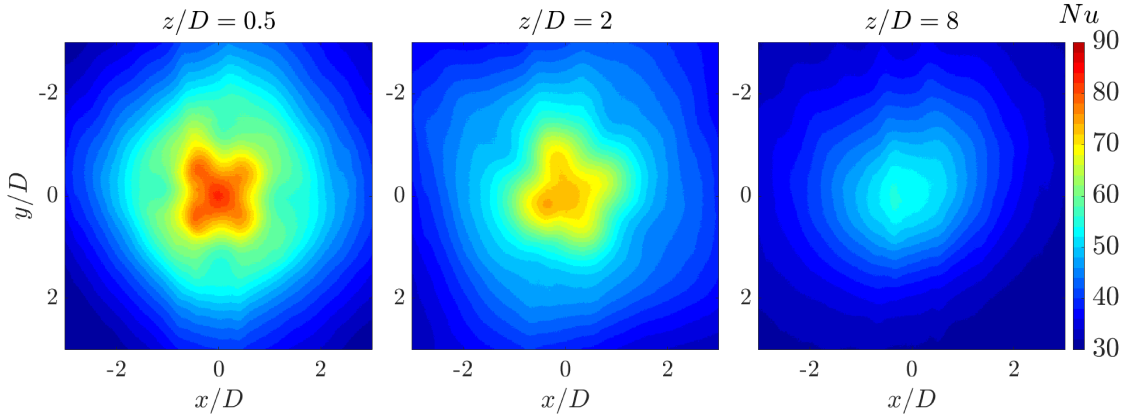


Figure 4.5: Heat transfer maps for plasma-based active swirler at $Re = 4400$

In the case of the plasma-based actuator (case B), the heat maps in Figure 4.5 show again a four lobe structure, consistent with the four pairs of electrodes composing the swirler, appearing from the lowest nozzle-to-plate spacings up to $z/D = 2$. This structure, however, is different than the multichannel, with a single stagnation zone

in the jet centerline, eliminating the local minimum present in the passive jet due to the walls of the insert. With increasing impinging distances, the maximum Nu values diminish and the lobe structure slowly fades into a circular shape, consistent with the behaviour previously observed for the passive swirler. Importantly however, the active swirler differs from the passive in the intensity of the Nusselt peaks, showing only a 21% increase for $z/D = 0.5$ and 10% for $z/D = 2$ compared to the round jet.

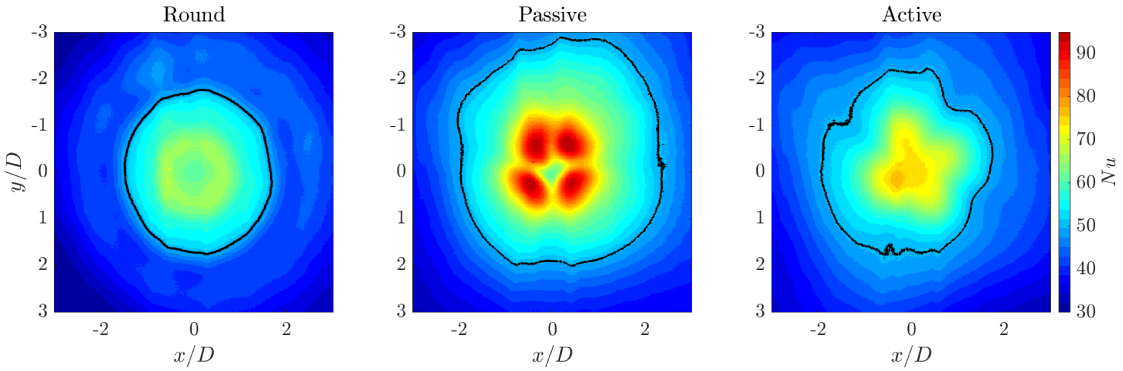
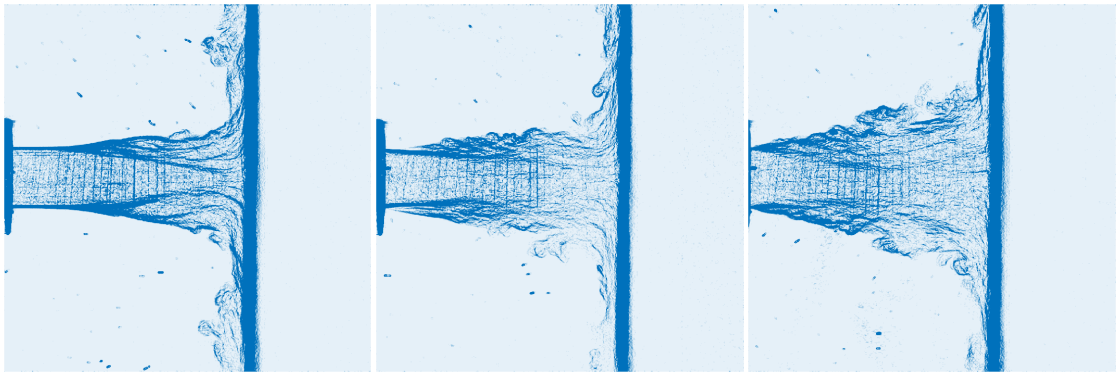


Figure 4.6: Heat transfer for the three configurations at $Re = 4400$, $z/D = 2$ with black isoline at $Nu = 50$

Compared with the round jet, both for the passive and active swirlers, the impingement region appears larger, as shown in figure 4.6, with the most significant enhancement observed within a radial distance of $r/D = 1.5$. This behavior is attributed to the increased radial spreading of the jet, which promotes a wider distribution of momentum over the impingement surface. As a result, the region affected by the jet is enlarged, leading to enhanced flow interaction in the vicinity of the stagnation point. The increased radial spread is also clearly visible in the flow visualizations presented in figure 4.7.

The snapshots shown in Figure 4.7, were acquired with a sCMOS camera and illustrate the development of the impinging jet at a nozzle-to-plate distance of $z/D = 4$ for the three configurations investigated. The plasma generated swirling jet exhibits a radial expansion earlier than both the baseline and passive configurations, indicating enhanced mixing and a more rapid breakdown of the potential core. The passive swirler also promotes radial spreading of the jet; however, the potential core remains longer and more pronounced than in the plasma actuated case.

The same overall description can be applied to the case C of the DBD-PA, with the difference of a slightly faster decrease of heat transfer with the increase of nozzle-to-plate spacings.



(a) round **(b)** passive **(c)** active

Figure 4.7: Snapshots at nozzle to plate distance $z/D = 4$.

4.2.2 Radial Nusselt distribution and standard deviation

Further insight is given by the radial Nusselt distributions and standard deviation on azimuthal paths and circular areas. Figure 4.8 shows the surface averaged Nusselt and percentage standard deviation radial distributions, as expressed in equations 3.11, 3.12. The image compares the circular jet (CJ), the plasma based active swirler (PA) and the multichannel passive swirler (MC) radial profiles. While the multichannel provides a consistent increase of heat transfer over r/D and z/D, figure 4.8 shows that the increase for the active swirler is more evident in the area close to the centerline and limited to short impinging distances. Combined with this small increase in heat transfer, the DBD-PA maintains uniformity over the area comparable with that of the round jet, opposed to a $5 - 10\%$ increase of the σ_{Nu} for the multichannel.

A similar result is provided by the azimuthally averaged Nusselt radial distributions and standard deviation (Eqs. 3.13, 3.14), as shown in figure 4.9. Here it can be clearly spotted the peak of Nu and its corresponding peak in azimuthal non-uniformity for the passive swirler around $r/D = 0.5$.

More in detail, $z/D = 0.5$ is the nozzle-to-plate spacing where the active swirler provides the most effect, especially in the central region, with only a small peak in $\sigma_{\langle Nu \rangle}$ around $r/D = 1$ due to the lobes generated by the four pairs of electrodes. This is also the distance where the passive siwrler provides the highest overall Nusselt value of $\langle Nu \rangle \sim 110$. However, after $r/D = 2.5$ all three testcases converge to similar values, with no noticeable effect of the swirl at higher radii.

At $z/D = 2$, the multichannel's heat transfer is consistently around 10% higher than both the plasma based and round jet over the full investigated r/D range, with these last two differing from one another only for the shape of the curve and a noticeable Nu increase in the central region for the PA.

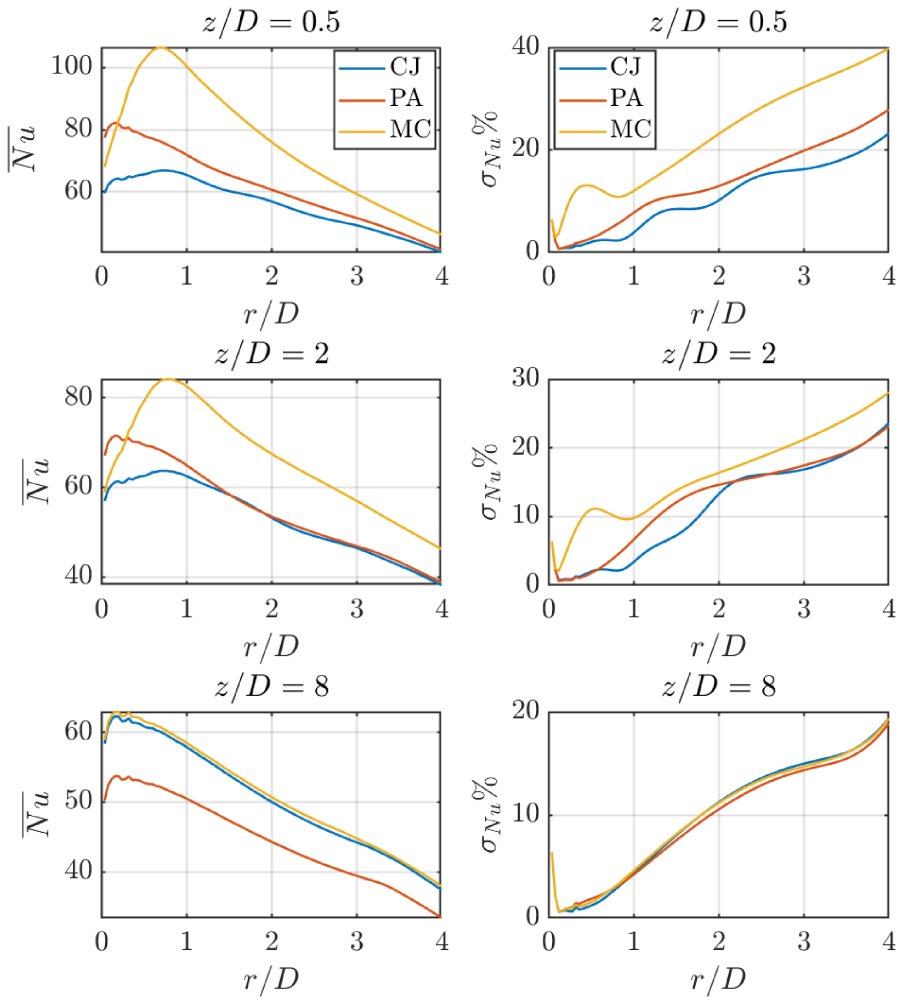


Figure 4.8: Surface averaged Nusselt number and percentage standard deviation radial profiles for CJ, MC, and PA

At the longest investigated impinging distance, $z/D = 8$, there is no noticeable difference between the multichannel and circular jet, while the plasma based swirling jet shows a decrease in heat transfer over all the impinged area.
The active swirler is very effective in the impinged area near the centerline, with surface averaged Nusselt number comparable or higher than the passive swirler for $r/D < 0.25$. This is due to the absence of the walls of the passive insert, that obstruct the flow in the jet axis. As shown in Figure 4.10, this advantage disappears at higher radii, due to the heat transfer peak in the four stagnation zones of the multichannel.
Despite the better performance, passive swirlers introduce additional flow resistance due to the presence of the insert within the nozzle, resulting in a 40% increase of

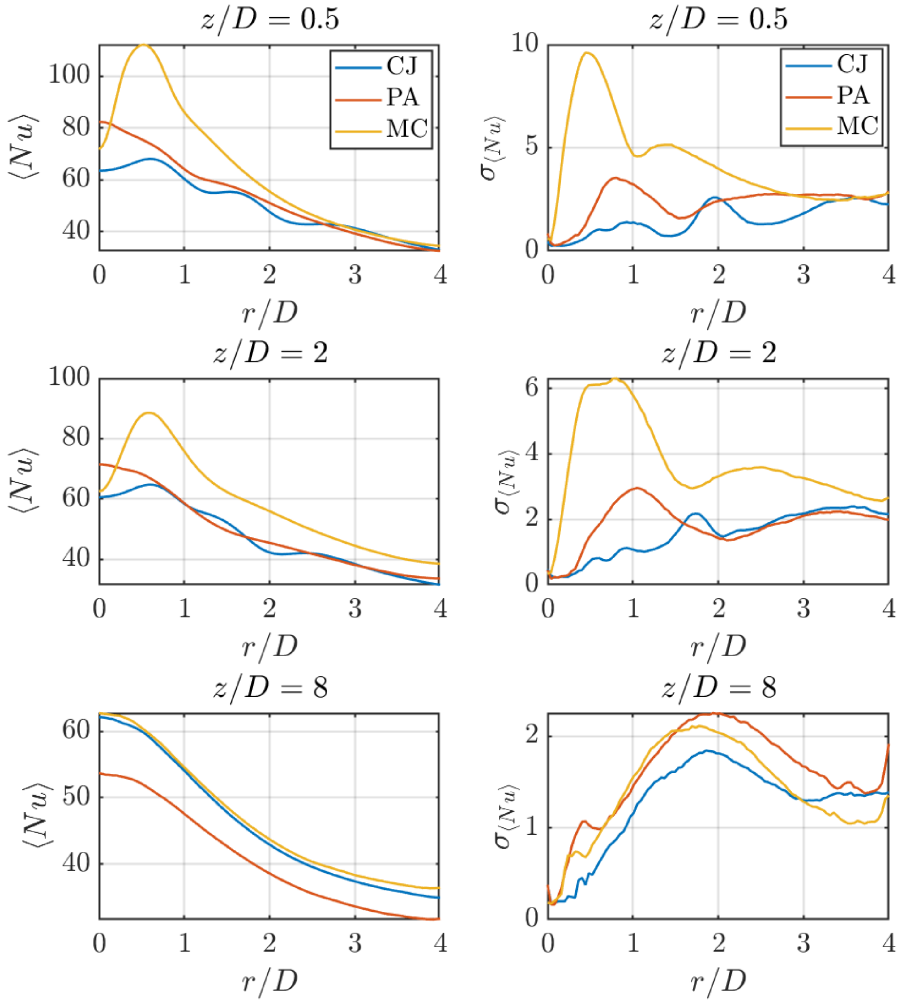


Figure 4.9: Azimuthally averaged Nusselt number and standard deviation radial profiles for CJ, MC, and PA

Δp over the nozzle. Conversely, the active solution does not provide internal flow obstructions, although it requires a modest electrical power input, with typical values as low as 25 W.

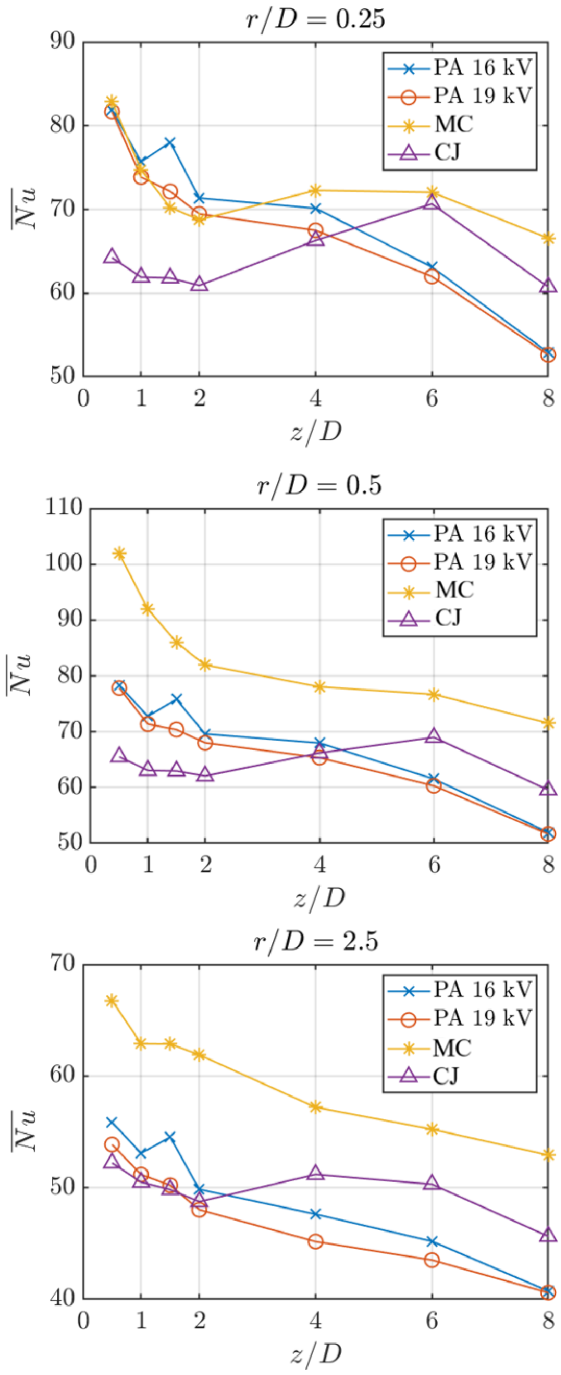


Figure 4.10: Surface averaged Nusselt number over a circular area at fixed radius $r/D = [0.25, 0.5, 2.5]$ as a function of z/D for PA swirler (case B and C), MC and CJ

Chapter 5

Conclusions

The present work investigated the heat transfer characteristics of impinging swirling jets generated by both passive and active swirl generation techniques. Quantitative infrared thermography was employed to evaluate the local convective heat transfer distributions on a heated thin-foil sensor, allowing a direct comparison between a conventional round jet, a passive helical multichannel swirler, and a plasma-based active swirler based on dielectric barrier discharge plasma actuators.

A preliminary validation of the experimental methodology was performed using a circular non-swirling impinging jet at Reynolds numbers of 4400 and 16000. The measured Nusselt number distributions reproduced the characteristic features reported in the literature, including the presence of annular heat transfer peaks at short nozzle-to-plate distances and the transition towards a bell-shaped profile at larger spacings. The observed influence of Reynolds number and impinging distance showed good agreement with previous experimental studies [35, 36], confirming the reliability of the measurement approach and data processing procedure.

The passive multichannel swirler produced the largest enhancement of heat transfer among the investigated configurations. At short nozzle-to-plate distances, the flow was divided into four distinct jets, generating four stagnation regions and peak Nusselt numbers up to 75% higher than those of the reference round jet. This enhancement remained significant over a wide radial range and persisted for intermediate nozzle-to-plate distances. However, the increased heat transfer was accompanied by a reduction in spatial uniformity and by a substantial pressure loss, with an approximately 40% increase in pressure drop across the nozzle.

The plasma-based active swirler generated a four-lobe heat transfer pattern associated with the arrangement of the DBD plasma actuators while maintaining a central stagnation region. Although the overall heat transfer enhancement was lower than that obtained with the passive swirler, the active configuration still achieved increases of approximately 21% and 10% relative to the round jet at (z/D = 0.5) and (z/D = 2), respectively. The effect of plasma actuation was found to

be concentrated primarily in the region close to the jet centerline, where the active swirler produced surface-averaged Nusselt numbers comparable to, or even greater than, those obtained with the passive insert.
An important outcome of the study is that the active swirler preserved several desirable characteristics of the conventional round jet. In contrast to the passive insert, plasma actuation introduced no flow blockage and maintained a level of heat transfer uniformity comparable to that of the baseline circular jet. The resulting heat transfer distribution was therefore more homogeneous than that produced by the passive swirler, while still providing a measurable enhancement of convective heat transfer.
Overall, the results demonstrate that plasma-based swirl generation represents a possible alternative to conventional passive swirlers for impinging jet heat transfer applications. While the passive insert remains more effective in maximizing local and area-averaged heat transfer, the active swirler offers a favourable compromise between heat transfer enhancement, spatial uniformity, and aerodynamic performance. These characteristics make DBD-plasma swirlers particularly attractive for applications where pressure losses and thermal uniformity are critical design requirements.
The active swirl generator investigated in the present work represents only one of the possible configurations achievable using DBD plasma actuators. During the course of this research, additional actuator designs were developed, including a five-electrode configuration and a longer actuator with an active length of 10 cm, compared to the 7 cm configuration employed in the present study. These designs provide promising opportunities for future investigations aimed at evaluating the influence of actuator geometry on the generated swirl intensity and the resulting heat transfer performance.
Furthermore, previous aerodynamic studies have demonstrated the feasibility of varying the actuation voltage and excitation frequency, as well as implementing sequential triggering strategies to actively control the generated flow field [22, 23]. While these operating conditions have been characterized from an aerodynamic perspective, their influence on impinging jet heat transfer has yet to be experimentally assessed, representing a natural continuation of the present work.
Finally, the experimental apparatus could be extended to investigate the fluid dynamic mechanisms responsible for the observed heat transfer behavior. By replacing the heated foil with a pressure sensitive surface instrumented with pressure taps and microphones, it would be possible to measure the pressure distribution and pressure fluctuations within the impingement region. Correlating these measurements with the heat transfer data would provide further insight into the relationship between the wall jet dynamics, coherent flow structures, and the resulting convective heat transfer.

Appendix A

Uncertainty propagation

The uncertainty associated with the experimental measurements was evaluated using the propagation of errors method proposed in [30]. This methodology provides an estimate of the uncertainty of a calculated quantity by combining the uncertainties of the independent measured variables from which it is derived.

Assuming that the measured quantities are independent and that their uncertainties are small, the uncertainty of a result $R = f(x_1, x_2, \ldots, x_n)$ can be estimated from a first order Taylor series expansion. The combined uncertainty is therefore expressed as

$$U_R = \sqrt{\sum_{i=1}^{n} \left(\frac{\partial R}{\partial x_i} U_{x_i} \right)^2}, \tag{A.1}$$

where U_R is the uncertainty associated with the calculated quantity, U_{x_i} is the uncertainty of the independent variable x_i, and $\partial R/\partial x_i$ is the corresponding sensitivity coefficient. This approach assumes that the individual uncertainties are uncorrelated and combine according to the root-sum-square (RSS) criterion.

In the present work, the quantity of primary interest is the local Nusselt number, which is evaluated from several experimentally measured quantities, including temperature, electrical power input, geometrical dimensions, and thermophysical properties. The uncertainty associated with the Nusselt number was therefore determined by propagating the uncertainties of all the independent variables entering its formulation according to Eq. (A.1).

Starting from the Nusselt equation, and it's associated uncertainty:

$$Nu = \frac{hD}{k_a} \tag{A.2}$$

$$\delta Nu = \sqrt{\sum \left(\frac{\partial Nu}{\partial x_i}\right)^2 \delta x_i^2} \tag{A.3}$$

the following derivatives of the parameters influencing the value of the Nusselt number were evaluated:

$$\begin{aligned}
\frac{\partial Nu}{\partial D} &= \frac{h}{k_a} \\
\frac{\partial Nu}{\partial k_a} &= -\frac{hD}{k_a^2} \\
\frac{\partial Nu}{\partial V} &= \frac{D}{k_a}\frac{I}{(T_w - T_{aw}) \cdot A^*} \\
\frac{\partial Nu}{\partial I} &= \frac{D}{k_a}\frac{V}{(T_w - T_{aw}) \cdot A^*} \\
\frac{\partial Nu}{\partial A^*} &= -\frac{D}{k_a}\frac{I \cdot V}{(T_w - T_{aw}) \cdot A^{*2}} \\
\frac{\partial Nu}{\partial k_f} &= -\frac{D}{k_a}\frac{s_f \nabla^2 T}{T_w - T_{aw}} \\
\frac{\partial Nu}{\partial s_f} &= -\frac{D}{k_a}\frac{k_f \nabla^2 T}{T_w - T_{aw}} \\
\frac{\partial Nu}{\partial k_p} &= -\frac{D}{k_a}\frac{s_p \nabla^2 T}{T_w - T_{aw}} \\
\frac{\partial Nu}{\partial s_p} &= -\frac{D}{k_a}\frac{k_p \nabla^2 T}{T_w - T_{aw}} \\
\frac{\partial Nu}{\partial \varepsilon} &= -\frac{D}{k_a}\frac{\sigma(T_w^4 - T_{amb}^4)}{T_w - T_{aw}} \\
\frac{\partial Nu}{\partial T_{amb}} &= \frac{D}{k_a}\frac{4\sigma\varepsilon T_{aw}^3}{T_w - T_{aw}} \\
\frac{\partial Nu}{\partial T_{aw}} &= -\frac{D}{k_a}\frac{q_j - q_k - q_r}{(T_w - T_{aw})^2}
\end{aligned}$$

and

$$\begin{aligned}
\frac{\partial Nu}{\partial T_w} &= \frac{\partial (D/k_a)}{\partial T_w} \cdot h + \frac{D}{k_a} \cdot \frac{\partial (h)}{\partial T_w} \\
\frac{\partial (D/k_a)}{\partial T_w} &= -\frac{2.9 \times 10^5 D}{131 \cdot T_w^{1.76}} \\
\frac{\partial h}{\partial T_w} &= \frac{q_j + q_k + \sigma\varepsilon(-3T_w^4 + 4T_{aw}T_w^3 - T_{amb}^4)}{(T_w - T_{aw})^2}
\end{aligned}$$

Appendix B

Nozzle flow characterization

An experimental correlation between the axial centerline velocity at the nozzle exit and the pressure drop through the nozzle was developed. The jet facility tested is the same described in section 3.1, including the feeding line with the pressure regulators and the pressure taps at inlet and outlet of the nozzle. The nozzle exit is completed with a single channel cylindrical short pipe of length $L = 7$ cm, recreating the circular jet condition. At nozzle exit $z/D = 0$ is positioned a pitot probe along the axial direction of the jet at its centerline. The pressure control valves allowed to test various flow conditions, characterized by the $\Delta p = p_{in} - p_{out}$ between inlet and outlet of the nozzle, recorded by the pressure taps. For each condition tested, in the range of Δp between 0 and 100 Pa, dynamic and static pressure is acquired via the pitot tube. The velocity is then obtained through equation B.1, where p_d and p_s are respectively the dynamic and static pressure.

$$V_x = \sqrt{\frac{2(p_d - p_s)}{\rho}} \tag{B.1}$$

From this data, a correlation between nozzle Δp and V_x was developed with a polynomial fitting, reported in equation B.2 and in figure B.1

$$V_x = 0.5117\Delta p^2 + 0.0682\Delta p - 0.2377 \tag{B.2}$$

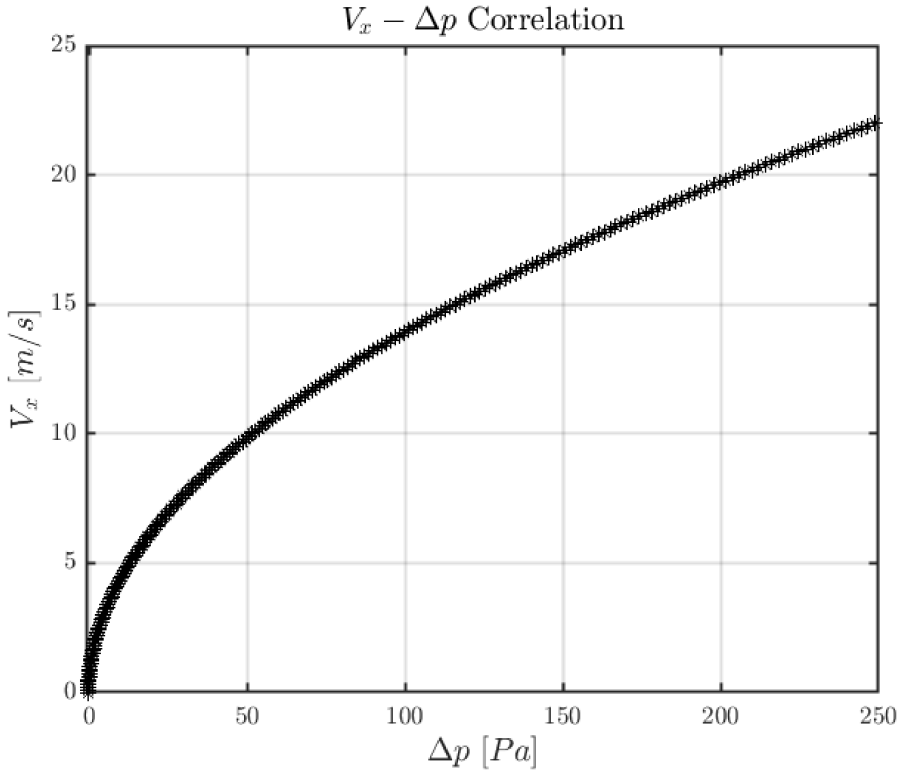


Figure B.1: $V_x - \Delta p$ correlation extended to a wider nozzle pressure drop range (0 to 250 Pa)

Appendix C

Flow visualization

In order to obtain qualitative visualizations of the flow field, a laser flow visualization setup was implemented. The jet facility employed for these measurements was the same as that used throughout the main experimental campaign, excluding the heat flux sensor and thermographic setup. The air supply line was equipped with a Laskin nozzle, shown in figure C.1. This is a device that acts as an atomizer and generates a fine mist of seeding particles and disperses them uniformly within the flow.

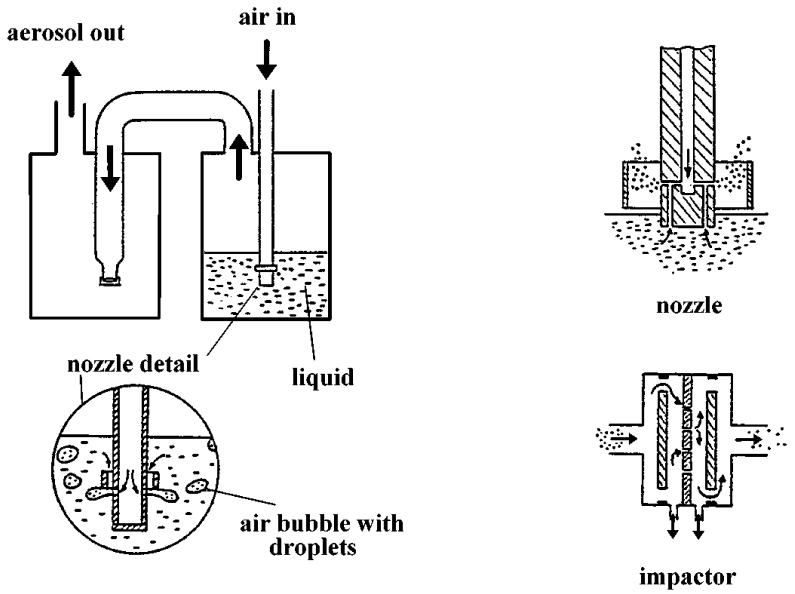


Figure C.1: Scheme of a Laskin nozzle reproduced from [38]

After exiting the nozzle, the seeded jet was illuminated by a laser sheet positioned vertically to delineate the yz plane in the jet's centerline. The suspended particles

scatter the incident laser light, making the flow structures visible. The scattered light was then recorded using an Andor Zyla 5.5 MP sCMOS camera, with sensor size of 2560 × 2160 pixels^2 and with pixel size of 6.5 µm, equipped with a Tokina ATX-I macro lense with 100 mm focal length and positioned orthogonally to the measurement plane. A sketch of the experimental setup is reported in figure C.2

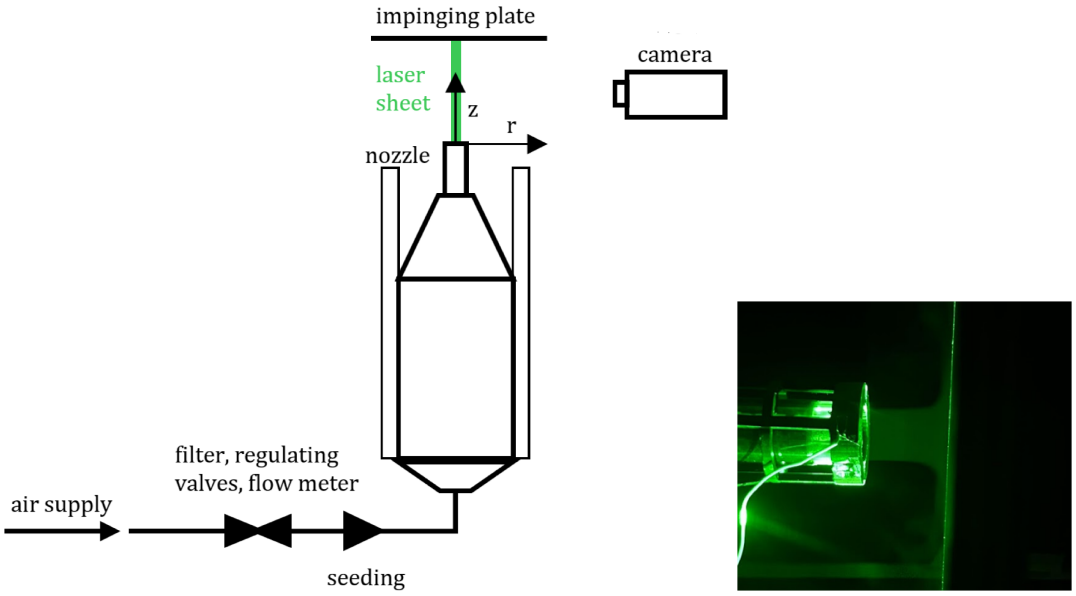


Figure C.2: Laser visualization experimental setup

For each analyzed case, 50 snapshots were acquired at a frequency of 20 Hz, and were used to compose video sequences. From these, representative images were selected and processed by computing the magnitude of the light intensity gradient, in order to highlight the contours of the flow structures. The objective of these measurements was to provide a qualitative visualization of the coherent flow structures generated by the different swirlers and to complement the quantitative heat transfer measurements presented in the main body of the thesis, highlighting the different jet spreading and formation of the characteristic jet regions for the different configurations tested

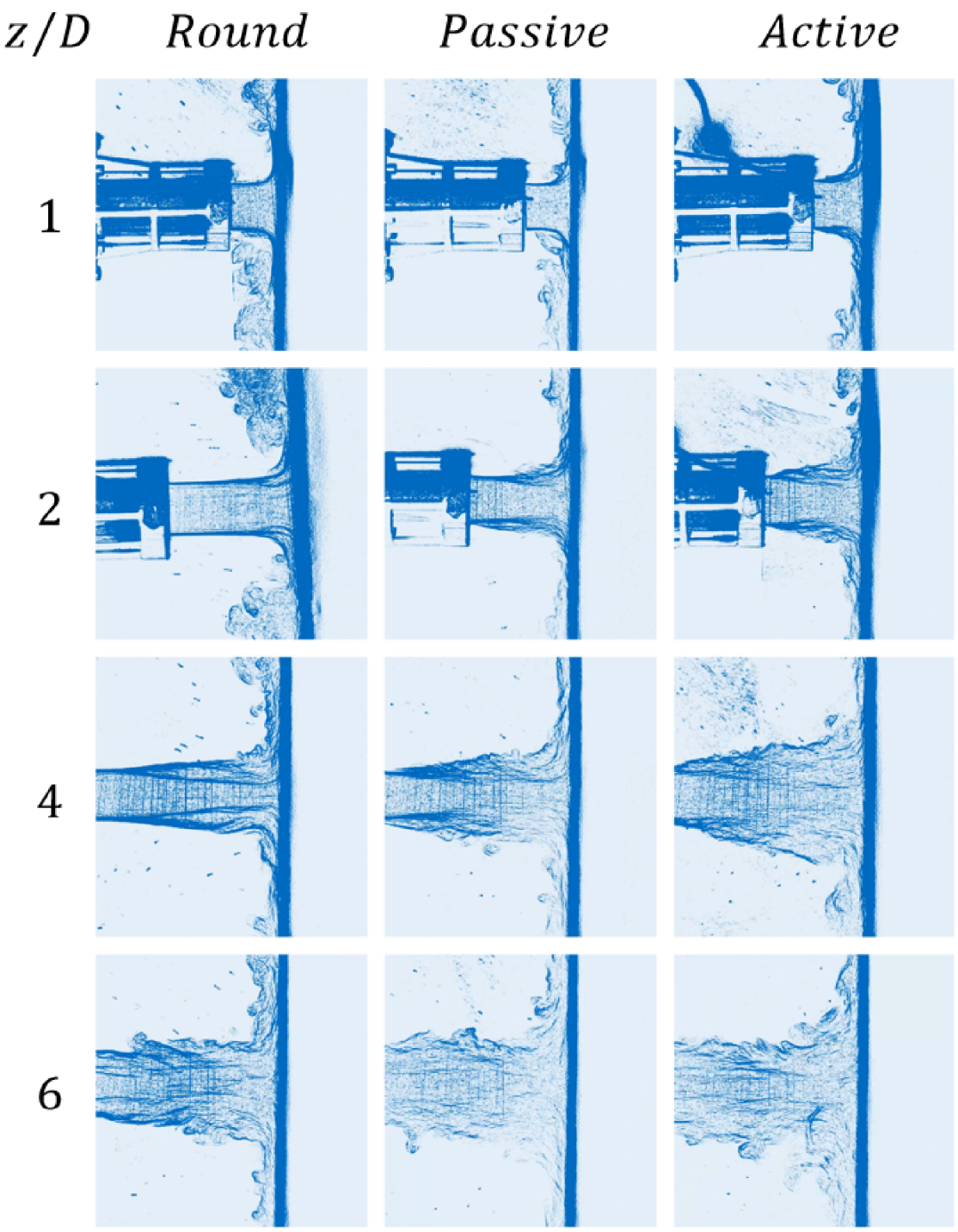


Figure C.3: Images of all investigated cases with laser visualization

References

[1] G. M. Carlomagno and A. Ianiro. «Thermo-fluid-dynamics of submerged jets impinging at short nozzle-to-plate distance: A review». In: *Experimental Thermal and Fluid Science* 58 (2014), pp. 15–35 (cit. on pp. 1, 2, 4, 9, 50).

[2] R. Viskanta. «Heat transfer to impinging isothermal gas and flame jets». In: *Experimental Thermal and Fluid Science* 6.2 (1993), pp. 111–134. ISSN: 0894-1777. DOI: https://doi.org/10.1016/0894-1777(93)90022-B (cit. on p. 2).

[3] A Ianiro and G. Cardone. «Heat transfer rate and uniformity in multichannel swirling impinging jets». In: *Applied Thermal Engineering* 49 (2012), pp. 89–98 (cit. on pp. 3–5, 21, 22, 40, 41, 50, 52).

[4] P Billant, J. Chomaz, and P Huerre. «Experimental study of vortex breakdown in swirling jets». In: *Journal of Fluid Mechanics* 376 (1998), pp. 183–219 (cit. on pp. 3, 5).

[5] G. Paolillo, C. S. Greco, T. Astarita, and G. Cardone. «Effects of the swirl number, Reynolds number and nozzle-to-plate distance on impingement heat transfer from swirling jets». In: *International Journal of Heat and Mass Transfer* 197 (2022) (cit. on pp. 4–6, 9, 10, 50).

[6] I. K. Toh, D. Honnery, and J. Soria. «Axial plus tangential entry swirling jet». In: *Experiments in Fluids* 48 (2010), pp. 309–325 (cit. on p. 4).

[7] H. Liang and T. Maxworthy. «An experimental investigation of swirling jets». In: *Journal of Fluid Mechanics* 525 (2005), pp. 115–159 (cit. on pp. 4, 5).

[8] Gang Li, Xi Jiang, Junqiang Zhu, Jinhu Yang, Cunxi Liu, Yong Mu, and Gang Xu. «Combustion control using a lobed swirl injector and a plasma swirler». In: *Applied Thermal Engineering* 152 (2019), pp. 92–102. ISSN: 1359-4311. DOI: https://doi.org/10.1016/j.applthermaleng.2019.02.042 (cit. on pp. 5, 6).

[9] X.Q. Huang, C.W. Leung, C.K. Chan, and S.D. Probert. «Thermal characteristics of a premixed impinging circular laminar-flame jet with induced swirl». In: *Applied Energy* 83.4 (2006), pp. 401–411. DOI: https://doi.org/10.1016/j.apenergy.2005.04.001 (cit. on p. 5).

[10] A. Giannadakis, K. Perrakis, and Th. Panidis. «A swirling jet under the influence of a coaxial flow». In: *Experimental Thermal and Fluid Science* 32.8 (2008), pp. 1548–1563. ISSN: 0894-1777. DOI: https://doi.org/10.1016/j.expthermflusci.2008.04.010 (cit. on pp. 5, 6).

[11] Gang Li, Xi Jiang, Yujun Zhao, Cunxi Liu, Qi Chen, Gang Xu, and Fuqiang Liu. «Jet flow and premixed jet flame control by plasma swirler». In: *Physics Letters A* 381.13 (2017), pp. 1158–1162 (cit. on pp. 5, 7, 42).

[12] Gang Li and Xi Jiang. «Effects of electrical parameters on theperformance of a plasma swirler». In: *Physica scripta* 94.9 (2019), p. 95601. DOI: 10.1088/1402-4896/ab170e (cit. on p. 7).

[13] Gang Li, Xi Jiang, Lei Jiang, Zhijun Lei, Junqiang Zhu, Yong Mu, and Gang Xu. «Design and experimental evaluation of a plasma swirler with helical shaped actuators». In: *Sensors and Actuators A: Physical* 315 (2020), p. 112250. ISSN: 0924-4247. DOI: https://doi.org/10.1016/j.sna.2020.112250 (cit. on pp. 7, 8).

[14] Francis F. Chen. «Special Plasmas». In: *Introduction to Plasma Physics and Controlled Fusion*. Cham: Springer International Publishing, 2016, pp. 333–353. ISBN: 978-3-319-22309-4. DOI: 10.1007/978-3-319-22309-4_9 (cit. on p. 13).

[15] Marios Kotsonis. «Diagnostics for characterisation of plasma actuators». In: *Measurement Science and Technology* 26.9 (Aug. 2015), p. 092001. DOI: 10.1088/0957-0233/26/9/092001 (cit. on pp. 14, 16–18, 20).

[16] Jochen Kriegseis, Bernhard Simon, and Sven Grundmann. «Towards In-Flight Applications? A Review on Dielectric Barrier Discharge-Based Boundary-Layer Control». In: *Applied Mechanics Reviews* 68.2 (July 2016), p. 020802. ISSN: 0003-6900. DOI: 10.1115/1.4033570 (cit. on pp. 14, 16–18).

[17] C. Enloe, T. McLaughlin, J. Gregory, R Medina, and W Miller. «Surface Potential and Electric Field Structure in the Aerodynamic Plasma Actuator». In: *46th AIAA Aerospace Sciences Meeting and Exhibit*. DOI: 10.2514/6.2008-1103 (cit. on p. 15).

[18] Tongkai Zhang, Yu Zhang, Qizheng Ji, Ben Li, and Jiting Ouyang. «Characteristics and underlying physics of ionic wind in dc corona discharge under different polarities*». In: *Chinese Physics B* 28.7 (July 2019), p. 075202. DOI: 10.1088/1674-1056/28/7/075202 (cit. on p. 15).

[19] Eric Moreau. «Airflow control by non-thermal plasma actuators». In: *Journal of Physics D: Applied Physics* 40.3 (Jan. 2007), p. 605. DOI: 10.1088/0022-3727/40/3/S01 (cit. on pp. 16–18).

[20] Philipp Warlitz, Marc T. Hehner, Saskia Pasch, Jacopo Serpieri, Thomas Blank, and Jochen Kriegseis. «On durable materials for dielectric-barrier discharge plasma actuators». In: *Sensors and Actuators A: Physical* 366 (2024), p. 114985. ISSN: 0924-4247. DOI: https://doi.org/10.1016/j.sna.2023.114985 (cit. on pp. 16, 20).

[21] David Ashpis, Matthew Laun, and Elmer Griebeler. «Progress toward Accurate Measurements of Power Consumption of DBD Plasma Actuators». In: Jan. 2012. DOI: 10.2514/6.2012-823 (cit. on pp. 18, 19).

[22] M. Zannone. «Plasma-based swirling jets». MA thesis. Torino: Politecnico di Torino, 2024 (cit. on pp. 20, 23, 33, 41, 42, 60).

[23] G. Putignano. «Passive and active (plasma based) swirling jets». MA thesis. Torino: Politecnico di Torino, 2025 (cit. on pp. 20, 21, 23, 33, 41–43, 60).

[24] G. M. Carlomagno and G. Cardone. «Infrared thermography for convective heat transfer measurements». In: *Experiments in Fluids* 49 (2010), pp. 1187–1218 (cit. on pp. 24, 28, 29).

[25] G. Cardone. «Quantitative infrared thermography in thermo-fluid-dynamics». In: (). URL: http://dx.doi.org/10.21611/qirt.1998.001 (cit. on p. 24).

[26] C. Ibarra-Castanedo and X. P. V. Maldague. *Handbook of Technical Diagnostics*. Berlin, Heidelberg: Springer, 2013. Chap. Infrared Thermography. URL: https://doi.org/10.1007/978-3-642-25850-3_10 (cit. on p. 24).

[27] G. M. Carlomagno, L. de Luca, G. Cardone, and T. Astarita. «Heat Flux Sensors for Infrared Thermography in Convective Heat Transfer». In: *Sensors* 14 (2014,). DOI: doi:10.3390/s141121065 (cit. on pp. 28, 29).

[28] T. Astarita, G. Cardone, G.M. Carlomagno, and C. Meola. «A survey on infrared thermography for convective heat transfer measurements». In: *Optics and Laser Technology* 32 (2000), pp. 593–610 (cit. on p. 29).

[29] T. Astarita and G. Cardone. «Thermofluidynamic analysis of the flow in a sharp 180° turn channels». In: *Experimental Thermal and Fluid Science* 20 (2000), pp. 188–200 (cit. on p. 30).

[30] S.J. Kline and F.A. McClintock. *Describing uncertainties in single-sample experiments*. Vol. 75. 1953, pp. 3–8 (cit. on pp. 32, 61).

[31] Umberto Cisotti, Theodore von Kármán, and Tullio Levi-Civita. «Vorträge aus dem Gebiete der Hydro-und Aerodynamik (Innsbruck 1922)». In: Springer, 1924, pp. 248–259 (cit. on p. 33).

[32] Shiyong Yao, Yong Guo, Nan Jiang, and Junjie Liu. «An experimental study of a turbulent jet impinging on a flat surface». In: *International Journal of Heat and Mass Transfer* 83 (2015), pp. 820–832. ISSN: 0017-9310. DOI: https://doi.org/10.1016/j.ijheatmasstransfer.2014.12.026 (cit. on p. 39).

[33] A.K. Gupta, D.G. Lilley, and N. Syred. *Swirl Flows*. Energy and engineering science series. Abacus Press, 1984. ISBN: 9780856261756 (cit. on p. 40).

[34] K. Jambunathan, E. Lai, M. A. Moss, and B. L. Button. «A review of heat transfer data for single circular jet impingement». In: *International Journal of Heat and Fluid Flow* 13.2 (Jan. 1992), pp. 106–115. DOI: 10.1016/0142-727X(92)90017-4 (cit. on pp. 49, 50).

[35] D. Violato, A. Ianiro, G. Cardone, and F. Scarano. «Three-dimensional vortex dynamics and convective heat transfer in circular and chevron impinging jets». In: *International Journal of Heat and Fluid Flow* 37 (2012), pp. 22–36. DOI: https://doi.org/10.1016/j.ijheatfluidflow.2012.06.003 (cit. on pp. 49, 50, 59).

[36] G. Cafiero, G. Castrillo, C. S. Greco, and T. Astarita. «Effect of the grid geometry on the convective heat transfer of impinging jets». In: *International Journal of Heat and Mass Transfer* 104 (2017), pp. 39–50. DOI: https://doi.org/10.1016/j.ijheatmasstransfer.2016.08.003 (cit. on pp. 49, 59).

[37] Sang-Joon Lee Jungho Lee. «Stagnation region heat transfer of a turbulent axisymmetric jet impingement». In: *Experimental Heat Transfer* 12.2 (1999), pp. 137–156. DOI: 10.1080/089161599269753 (cit. on p. 50).

[38] A Melling. «Tracer particles and seeding for particle image velocimetry». In: *Measurement Science and Technology* 8 (1997), pp. 1406–1416 (cit. on p. 65).